# Laminin-defined Mechanical Status Modulates Retinal Pigment Epithelium Functionality


**Authors**

Aleksandra N. Kozyrina[1, 2, 7], Teodora Piskova[1, 2, 7], Francesca Semeraro[1, 2], Iris C. Doolaar[3,4], Taspia Prapty[1, 2], Tamás Haraszti[3, 4], Maxime Hubert[5, 6], Reinhard Windoffer[2], Rudolf E. Leube[2], Ana-Sunčana Smith[5, 6] and Jacopo Di Russo[1, 2, 3*]

**Affiliations**

[1]Interdisciplinary Centre for Clinical Research, RWTH Aachen University, Pauwelstrasse 30, 52074 Aachen, Germany.

[2]Institute of Molecular and Cellular Anatomy, RWTH Aachen University, Wendlingweg 2, 52074 Aachen, Germany.

[3]DWI – Leibniz-Institute for Interactive Materials, Forckenbeckstrasse 50, 52074 Aachen, Germany.

[4]Institute for Technical and Macromolecular Chemistry, RWTH Aachen University, Worringerweg 1-2, Aachen D-52074, Germany.

[5]PULS Group, Department of Physics and Interdisciplinary Center for Nanostructured Films, Friedrich-Alexander University of Erlangen-Nürnberg, 91058 Erlangen, Germany.

[6]Group for Computational Life Sciences, Division of Physical Chemistry, Rudjer Bošković Institute,10000 Zagreb, Croatia.

[7]These authors contributed equally to this work

*Corresponding author jdirusso@ukaachen.de



**Classification**

Biological Science, Biophysics and Computational Biology

**Keywords**

Laminin; Mechanical Homeostasis; RPE; Bruch's Membrane

## Significance

In the retina, the retinal pigmented epithelium (RPE) is responsible for the daily phagocytosis of photoreceptor cell fragments, a process vital for visual function. Along the visual axis, there is a natural decrease in the ratio of photoreceptors to RPE cells, indicating a decrease in RPE functional demand. This study reveals that the density of laminins in RPE basement membrane also diminishes along this axis, critically influencing RPE function by regulating its contractility. For the first time, we demonstrate the presence of a laminin-defined mechanical gradient within the RPE, which determines its capacity to support photoreceptor cells. Our findings highlight the importance of mechanical properties as a key factor in visual function, offering new insights into retinal health and disease.


## Abstract

Epithelial cells are highly interconnected, whereby they acquire mesoscale mechanical properties to accomplish specific tissue functions. In homeostasis, this mechanical status can be summarised as mechanical homeostasis, regulated by the balance of intercellular tension and extracellular matrix adhesion forces. In the outer retina, the significance of this force balance and its consequences for vision remains poorly understood. We found that the density of basement membrane laminins modulates the level of retinal pigmented epithelium contractility, which directly controls its efficiency in phagocytosing photoreceptor outer segments. *In vivo*, the density gradient of laminins follows retinal functional demand, supporting the physiological role of laminins in controlling epithelial mechanical homeostasis. Our data suggest that laminin density and isoform heterogeneity can differentially engage integrins β1 and β4, the ratio of which determines the contribution of actin vs keratin cytoskeleton in balancing tissue mechanics. With this work, we suggest that the extracellular matrix-defined mechanical status of retinal pigmented epithelium is a novel parameter for visual function.

# MAIN TEXT

## Introduction

The mechanical properties of any tissue define its function and state (*1*, *2*). In a homeostatic state, these mechanical features are maintained in a preferred range for optimal activity, also known as tissue mechanical homeostasis (*3*). One of the main players in defining the mechanical homeostasis of tissues is its extracellular matrix (ECM) composition (*4*, *5*).

In the retina, the most prominent ECM structure is the Bruch's membrane, situated at its outermost part, also known as outer retina (*6*). The Bruch's membrane favors nutrient exchange between the choroid vessels and the retina, and distally, the basement membrane layer provides structural support and adhesion to the retinal pigment epithelium (RPE). The RPE is a postmitotic cell monolayer which directly interfaces with the light-detecting neural tissue. In the developing eye, the RPE organizes the retina (*7*, *8*), while in the adult, it plays a key role in the visual cycle (*9*, *10*). One of the main activities of RPE cells is the daily phagocytosis of shed photoreceptor cell fragments, therefore mediating the constant renewal of their light-sensitive outer segments and ensuring photoreceptor lifespan and light sensitivity (*11–13*). The number of photoreceptor outer segments (POS) per RPE cell is not constant within the eye, with an average of 25-30 POS per RPE cell in the central and macular area and decreasing towards the periphery (~ 15 POS) (*14*), indicating a gradient of functional demand.

RPE cells are polygonal in shape and tightly adhere to each other: they arrange as a honeycomb-like structure in the center, which gradually shifts to a more elongated and less organized structure towards the retinal periphery, which suggests a change in its mechanical status (*15–17*).

Although the Bruch's membrane is known to spatially vary along the visual axis (*6*), it remains an open question how this influences RPE mechanical homeostasis. Here, we hypothesize that the spatial variation of Bruch's membrane cues controls RPE mechanical status and region-dependent functional capacity.

In this work, we find that the relative density of the basement membrane laminin 511 and 332 defines the level of RPE contractility, which directly controls its functional capacity. At low density, laminin 511 promotes high contractility in RPE, which differs from laminin 332 due to a lower integrin β4 vs β1 engagement. *In vivo*, we find that the density gradient of these laminin isoforms corresponds to changes in RPE mechanical status and functional demand.

These findings, for the first time, underline the importance of mechanical homeostasis in RPE and, in general, in the outer retina. The significance of RPE mechanical status for visual function in adults opens the question of its role in aging and sight-threatening diseases such as (high) myopia and age-related macular degeneration. Finally, this study could incentivize a larger use of Rho kinase inhibitors, currently used as anti-glaucoma medications, for other retinal diseases.

## Results

### Mechanical status of the RPE correlates with biochemical heterogeneity of Bruch's membrane.

To understand the possible relation between RPE mechanical status and Bruch's membrane biochemical and mechanical cues, we characterized the outer retina of adult mice (25-30 weeks) (Fig 1). Bruch's membrane, retinal complexity and function have been described in relation to the visual axis (*14*, *17*). In both mice and humans, the central region (macula in humans) exhibits the highest density of photoreceptor cells and the highest photoreceptor to

RPE ratio. This ratio gradually decreases with the visual axis, signifying a reduction in RPE functional demand (*14*). Hence, as previously shown (*15–17*), we identified three regions with respect to the radial distance from the optic nerve: center (300-1200 µm), mid periphery (1200-2000 µm) and far periphery (2000-3000 µm) (Fig. 1 A). We observed a substantial difference in the organization of RPE cells along the radial distance (Fig. 1 A), consistent with previous reports (*15–17*). From a classic honeycomb arrangement in the center, the RPE gradually changes to a monolayer consisting of more elongated cells at the far periphery (Fig. 1 A; sup fig. 1 A, D) (*15–17*).

The topology and morphology of an epithelial monolayer define its mechanical properties (*18–20*). Hence, we performed morphometric characterization of RPE cells in the different regions of the retina (Fig.1 B - D, sup. fig. 1 A - H). RPE cells have the largest area and perimeter in the central region ($\langle A \rangle = 469\ \mu m^2$; $\langle P \rangle = 84\ \mu m$), whereas they become smaller towards the mid periphery ($\langle A \rangle = 349\ \mu m^2$; $\langle P \rangle = 74\ \mu m$) and far periphery ($\langle A \rangle = 343\ \mu m^2$; $\langle P \rangle = 75\ \mu m$) (Sup. fig.1 F, G). Next, to better quantify the mechanics of this differential cell arrangement, we calculated the shape factor for each cell, defined as the cell perimeter P divided by the square root of the corresponding cell area A. This density-independent shape factor has been theorized to describe epithelial rigidity based on the balance between cortical tension and cell-cell adhesion energy, with lower values where the first element is more prominent (*21*). Our data show an average value in the retinal central region of 3.8, which gradually increases till reaching values over 4.0 at the far periphery. This implies a gradual increase of intercellular tension, coinciding with the decreasing RPE functional demand (Fig. 1 B, C, sup. fig. 1 E) (*14*). Additionally, the comparison of the cellular nuclear geometry shows a reduced roundness and circularity corresponding to a higher aspect ratio towards the far periphery, supporting the existence of different levels of intracellular strain (sup. fig. 1 I - K). Finally, we noticed the presence of two distinct cell populations in the center and mid periphery, visible when cell area and cell perimeter distributions are normalized and compared (Fig. 1 D, sup. fig. 1 H). Hence, we compared the topological relations of RPE cells across retinal regions by plotting the rescaled cell areas and perimeters as a function of the number of neighbors (respectively Lewis' law (*22–25*) and Desh's law (*26*)) (Fig. 1 E, sup. fig. 1 L). Both comparisons show different curve behavior in the retinal regions, especially evident between the far periphery and other regions.

To gain further insight into monolayer topology, we then correlated the number of neighbors *n* of each cell and the average number of neighbors *m(n)* of any adjacent cells to the first with *n* sides (Aboav-Weaire's laws) (Fig. 1 F) (*27–29*). This relation describes the mean number of neighbors that neighboring cells have via the topological parameter *b(n)* (see method section). The different regions show a linear relationship, as in any functional epithelium (*20*, *27–29*). Nevertheless, a shift is visible between values corresponding to retina regions, suggesting a topological variation of RPE from the center to the far periphery (Fig. 1 F, sup. fig. 1 M). Altogether, the extensive image-based morphometric and topological analyses (of more than 5500 cells from three mice – see method section)

strongly support the existence of different mechanical status in the monolayer from the retinal central region to the far periphery.

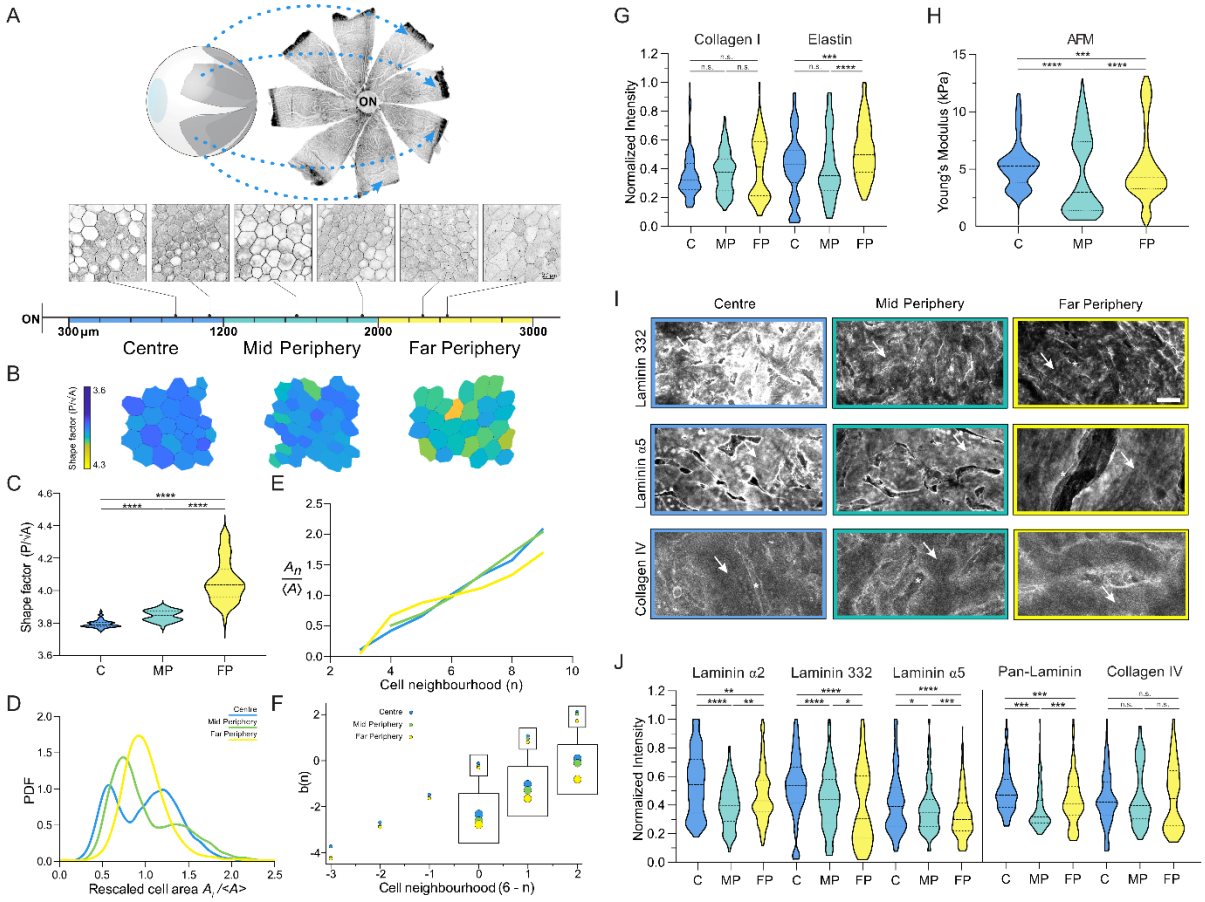


**Fig. 1. Spatial heterogeneity of murine retinal pigment epithelium topology and Bruch's membrane composition.** **(A)** Murine retina flat mount indicating the regions used for analyses and representative F-actin staining of RPE. The regions were defined by the distance from the optic nerve head: center (300 – 1200 µm), mid periphery (1200 – 2000 µm) and far periphery (2000 – 3000 µm). **(B)** Representative cell shape index maps for the three regions. The shape index is identified as the perimeter divided by the square root of the area for each cell. **(C)** Violin plot of mean RPE shape factors from the different regions of the eye analyzed from 7 mice. **(D)** The probability density function (PDF) of the rescaled cell areas defined by $A_i/\langle A \rangle$, $A_i$ being the individual cell area and $\langle A \rangle$ being the average cell area within a given image. More than 5500 cells were analysed from 3 mice. **(E)** Lewis' law representing the relationship between rescaled cell area and neighborhood varying for three different regions from 3 mice. **(F)** Aboav-Weaire's laws showing the variation of the topological parameter b(n) depending on the number of neighbors for each neighboring cell between different retinal regions from 3 mice. **(G)** Violin plots of mean fluorescence intensity of interstitial matrix components of the Bruch's membrane. Data were collected from 3 mice and normalized to the highest intensity per mouse. **(H)** Violin plots of the regional Young's modulus of the Bruch's membrane from 5 mice. **(I)** Representative immunofluorescent images of the Bruch's membrane stained for laminin 332, laminin α5 and collagen type IV. Arrows and stars indicate RPE basement membrane surface and preparation artefacts respectively. Scale bar 20 µm. **(J)** Violin plots of mean fluorescence intensity of basement membrane components: laminin α2, laminin 332, laminin α5, pan-laminin, and collagen type IV. Each region contains the quantification of at least 7 sectors from a minimum of 3 to 6 mice. The data were statistically tested with Mann-Whitney test: *$p < 0.05$; ** $p < 0.01$; *** $p < 0.001$; **** $p < 0.0001$; n.s. = not significant.

To determine whether this mechanical gradient is influenced by environmental cues, we next quantified the distribution of mechanical and biochemical cues stemming from the Bruch's membrane. In the epithelial ECM, mechanical cues are mostly determined by the composition and crosslinking density of the interstitial matrix (*5*). Therefore, we used confocal microscopy and immunofluorescence staining to quantify the relative amount of collagen type I and elastin present in the Bruch's membrane along the different regions. The average fluorescence intensity quantification of the retina's central, mid peripheral, and far peripheral regions were comparable with the data reported in the literature (*30*, *31*) (Fig. 1 G). Furthermore, we measured the Young's modulus of the Bruch's membrane in different

regions using atomic force microscopy (AFM) and indenting into the decellularised ECM by ~ 200 nm. The quantification resulted in a highly variable distribution of the data, with the center having the most frequent (mode) stiffness of 5.5 kPa, the mid periphery 1.5 kPa and the far periphery 4 kPa (Fig. 1 H). This biphasic stiffness trend suggests that ECM mechanical cues may not be the primary factor governing RPE mechanical homeostasis concerning functional demand.

From the biochemical point of view, the basement membrane regulates epithelial homeostasis, with different laminin isoforms playing a key role (*5*). Thus, we characterized the composition and relative amount of the main basement membrane components in the Bruch's membrane, namely laminins and collagen type IV (Fig. 1 I, J). Notably, we detected a significant difference in the relative amount of laminin isoforms along the visual axis, whereas collagen type IV remained unchanged. This supports the idea of the importance of laminins in the differential biochemical signaling to the RPE. Among the laminin isoforms detected in Bruch's membrane, we noticed a biphasic trend for laminin α2-containing isoforms, with higher (fluorescence) intensity in the center and far periphery and lower in the mid periphery. Laminin 332 and isoforms containing laminin α5 had the highest (fluorescence) intensity in the center that gradually diminished towards the periphery (Fig. 1 I, J), following photoreceptor density and functional demand. No laminin α1- or α4-containing isoforms were detected.

Altogether, the characterization of the murine outer retina suggests a possible relationship between the relative density of Bruch's membrane's laminins and region-dependent RPE mechanical status.

**Laminin 511 density influences contractility levels in RPE monolayers.**

The characterization of RPE cell topology and morphology in the retina suggested a relationship between laminin density in the basement membrane and monolayer mechanical status. To dissect the nature of this relationship, we established a bottom-up approach to scrutinize the role of the specific laminin isoforms and their density gradient. Human induced pluripotent stem cell-derived RPE (hiPSC-RPE) cells have already been successfully employed to model mature RPE and to study their functionality (*32*, *33*). Hence, we used hiPSC-RPE cells to obtain monolayers on polyacrylamide (PAA) hydrogels with 4 kPa Young's modulus to best mimic Bruch's membrane stiffness. hiPSC-RPE cells adhere and form a monolayer when seeded on PAA gels coated with different concentrations of laminin 511 (composed by laminin α5, β1 and γ1) and laminin 332, both in combination with collagen type IV (Sup. fig. 2 A). The gels were functionalized according to the method described in Przybyla et al. (*34*) with specific concentrations of laminin, reaching saturation at a coating concentration of around 20 µg/ml (Sup fig. 2 C). The advantages of PAA gel as a culture substrate are its defined stiffness (Youngs's modulus of the gel) and the protein-repellent nature of the polymer (*35*), allowing control over the biochemical cues originating from the coating. In fact, the staining for fibronectin confirmed the absence of aberrant deposition of ECM proteins by the cells while cultured (Sup. fig. 2 D). After a week of culture, hiPSC-RPE cells reach a low proliferative state (less than 8% in 24h) and form a columnar (junctional height ~10 - 15 µm) and polarized monolayer, as shown by the presence of apical microvilli (Fig. 2 A – D, sup. fig. 2 B). Due to this reductionistic approach, certain coating conditions were not permissive to obtain mature and intact RPE monolayers, such as laminin 511 and collagen type IV alone or laminin 211 (composed by laminin α2, β1 and γ1) also in combination with collagen type

IV (Sup. fig. 2 A, E and F). In conclusion, this reductionistic approach suggests that mainly laminin 511 and 332, but not laminin 211, support RPE adhesion *in vivo*.

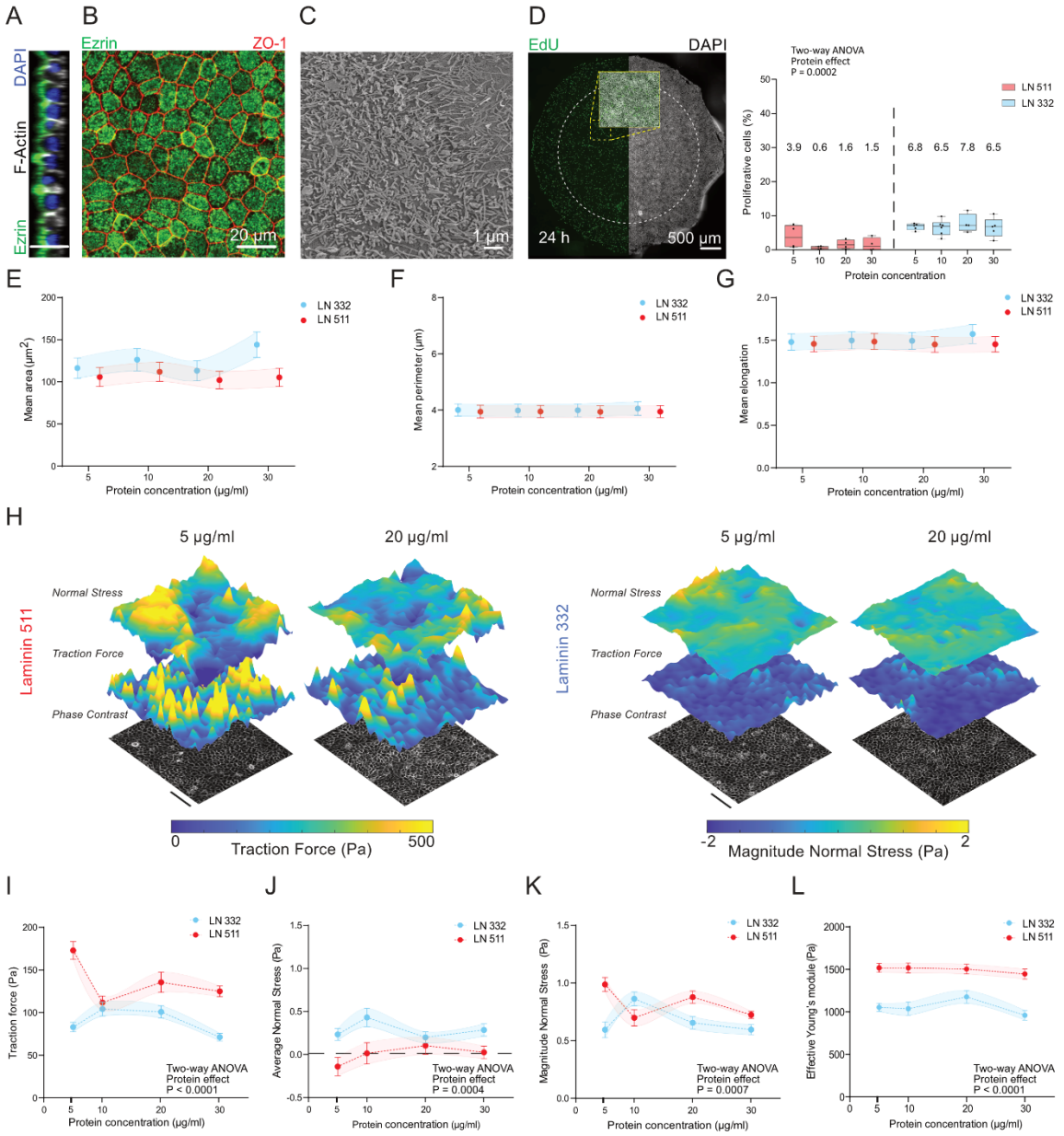


**Fig. 2. Reductionistic approach reveals the effect of laminin density on RPE biomechanics.** hiPSC-derived RPE obtained on PAA gel with Young's modulus of 4 kPa coated with laminin 511 or laminin 332 in the presence of collagen type IV. After one week in culture, cells form a polarized monolayer as observed in a confocal cross-section stained for the microvilli marker Ezrin **(A),** mature tight junctions (ZO-1) **(B),** and distinct apical microvilli as observed in the scanning electron micrograph of the monolayer surface **(C)**. DAPI staining marks the nuclei. **(D)** Cellular proliferation rate within 24 h obtained using EdU labelling assay for cells cultured on the PAA gel surface. A representative picture of the gel overview indicates the number of proliferating cells within one gel (left). The ratio of nuclei with incorporated EdU (per cent of proliferative cells) was quantified by the fluorescent signal in the central region of the gel to avoid possible edge effects (white circle). The data show average values ± SEM from at least 4 independent experiments. Statistic was performed using a mixed-effects model (REML) with the Geisser-Greenhouse correction, Tuckey's multiple comparisons test. Morphometric analyses of the cells reveal the absence of significant difference in cellular mean area **(E)**, mean perimeter **(F)** and mean elongation **(G)** between different laminin isoforms and densities from 3 independent experiments. **(H)** Representative traction force and monolayer stress profiles for different coating conditions and their quantifications **(I, J and K)** show a significant increase in contractility of RPE monolayers at the lowest laminin 511 density**. (L)** Quantification of the effective Young's modulus of the apical side of monolayer in different conditions. Data are shown as average ± SEM from at least 4 independent experiments. Statistical analyses were performed using a mixed-effects model (REML) with the Geisser-Greenhouse correction, Tuckey's multiple comparisons test.

Next, following the logic of a comparative approach between *in vivo* and *in vitro* systems, we performed morphometric and topological analyses of the monolayers obtained on the different laminin isoforms and densities. *In vivo,* these analyses functioned as indicators of RPE mechanical status. Nevertheless, *in vitro,* the quantification revealed a stable relationship among all laminin densities and isoforms, excluding their direct role in controlling monolayer morphology and topology (Fig. 2 E - G, sup. fig. 3 A - C). However, we wondered if those laminin coatings may affect contractile forces of the monolayer. We used traction force and monolayer stress microscopy to quantify RPE cell-matrix traction forces and cell-cell stresses in different conditions (Fig. 2 H - K). The quantifications revealed an overall ability of laminin 511 to promote higher traction forces compared to laminin 332 (Fig. 2 H, I), with the largest difference recorded at the lowest laminin density (170 Pa vs 80 Pa at 5 µg/ml) (Fig. 2 I). Next, we used the information on the traction forces and monolayer height (Sup. fig. 2 B) to calculate intercellular normal stresses in the different conditions as previously shown (*36*, *37*) (Fig. 3 H, J and K). Similarly, we observed a significant difference in the overall monolayer absolute stresses at the lowest coating density of laminins (5 µg/ml) with an average of ~1 Pa for laminin 511 and 0.6 Pa for laminin 332 (Fig. 2 K). As expected, the stress vectors exhibit an average close to 0 Pa for both coatings and densities, indicating that monolayers are nearly in equilibrium despite the variations in absolute contractility (Fig. 2 J). The difference in traction and stress at the lowest laminin 511 density hypothetically might be caused by a gradual increase in cell adhesion to collagen type IV, which remained constant across the conditions. We therefore tested the effect of collagen type IV on monolayer traction forces using laminin 332 as a control since laminin 511 alone does not support the formation of a monolayer (Sup. fig. 2 E). The quantification shows an overall decrease (~ 40%) of traction in the presence of collagen type IV (Sup. fig. 3 D), excluding the role of collagen type IV for the observed increased traction at the lowest laminin 511 density. Moreover, the clear distinction in traction between laminin 511 and laminin 332 strengthens the conclusion that the observed changes are exclusively laminin-induced.

Finally, we wanted to understand if the coating density could generally impact RPE cell surface stiffness, which may regulate its apical interaction with the neural retina. Therefore, we performed nanoindentation of RPE cells within the monolayers using a spherical probe of approximately 10 µm radius and quantified the average Effective Young's modulus of the monolayers (Fig. 2 L). The data show that RPE monolayers on laminin 511 are stiffer (~1.5 kPa) compared to laminin 332 (~1 kPa) regardless of the protein surface density.

Altogether, the biomechanical characterization of our model clearly indicates a divergent effect of the low density of laminin 511 versus laminin 332 on the overall RPE mechanical balance, promoting an increased contractility of the monolayer on laminin 511.

**Laminin-defined traction levels modulate RPE efficiency to phagocyte photoreceptor outer segments.**

Epithelial contractility levels have been shown to directly influence tissue functionality and reactivity (*36–43*). Therefore, considering the difference in RPE mechanics on lower laminin density, we wondered if there is any direct relationship between the monolayer mechanical status and its functional capacity. To understand this, we tested the ability of RPE monolayers on PAA gels to perform their fundamental physiological function: to bind and phagocyte POS fragments, which were isolated from porcine eyes and fluorescently labeled with FITC (Fig. 3 A - C). The quantification shows that, overall, at high laminin coating density (10 - 30 µg/ml) there is a comparable efficiency of phagocytosis between laminin 332 and 511, whereas a divergence is detected at the coating density of 5 µg/ml with reduced efficiency of RPE on laminin 511 (~50 %) (Fig. 3 B, C). These results highly

correlate with the traction force levels in RPE monolayers, suggesting a cause-effect relation between laminin-defined traction and RPE functional capacity. Hence, we addressed whether the efficiency of POS phagocytosis is directly affected by the level of RPE contractility independently of the biochemical nature of ECM adhesion (i.e., laminin isoforms or density) (Fig. 3 D - J).

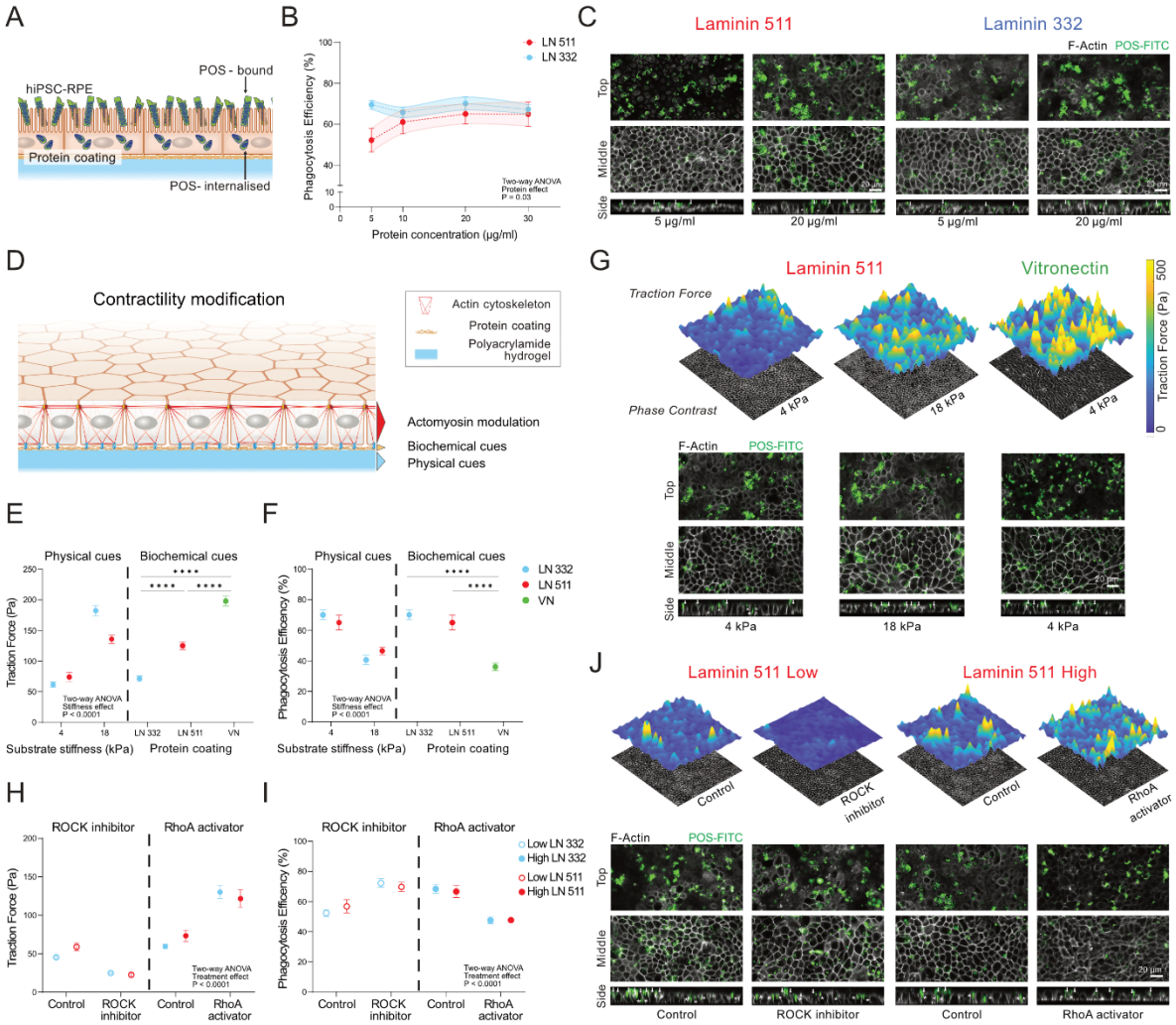


**Fig. 3. Laminin-defined RPE contractility modulates POS phagocytosis. (A)** Schematic representation of the photoreceptor outer segment internalization assay on RPE monolayer. **(B)** Average phagocytosis efficiency ± SEM for different laminin isoforms and their coating conditions from at least 4 independent experiments. The phagocytosis efficiency is defined as the amount of internalized POS divided by total POS. Statistical significance was tested using a mixed-effects model (REML) with the Geisser-Greenhouse correction, Tuckey's multiple comparisons test. **(C)** Representative confocal images of the hiPSC-RPE cells on PAA hydrogel with laminin 511 or laminin 332 coating (in the presence of collagen type IV). The top row indicates FITC-labelled POS fragments at the apical surface of the cells. The middle row represents an optical section of the cell monolayer with POS fragments inside. The results of the POS phagocytosis assay are visible in the orthogonal projections (bottom row) where arrows and stars indicate bound and internalized POS respectively. **(D)** Schematic representation of the experimental strategy to modulate monolayer contractility. Quantification of mean traction forces **(E)** and phagocytosis efficiency **(F)** ±SEM in RPE upon different ECM physical (stiffness) and biochemical cues (coating). PAA gels were coated with laminin 511 (LN 511) or laminin 332 (LN 332) (in the presence of collagen type IV) or with vitronectin (VN). ****p<0.0001 using mixed-effects model (REML) with the Geisser-Greenhouse correction, Tuckey's multiple comparisons test (physical cues) and Mann-Whitney test (biochemical cues). **(G)** Representative traction force plots and immunofluorescent images of POS internalization assay upon different physical or biochemical cues. Drug treatment affecting actomyosin contractility levels using ROCK inhibitor and RhoA activator shows inverse dependence between the level of monolayer contractility (traction forces) **(H)** and its ability to phagocyte POS fragments **(I)**. Data are shown as mean ± SEM. ****p<0.0001 using mixed-effects model (REML) with the Geisser-Greenhouse correction, Tuckey's multiple comparisons paired test. **(J)** Representative traction force plots and immunofluorescent images of POS internalization assay upon drug treatment.

To systematically adjust the traction force, we decided to tune either the ECM physical cues (i.e., hydrogel stiffness) or the biochemical nature of adhesion (i.e., laminins vs vitronectin) (Fig. 3 D). We then assessed the RPE efficiency in internalizing POS by comparing it with the maximum efficiency observed in RPE on laminins. First, we obtained RPE monolayers on stiffer hydrogels (18 kPa) coated with laminin 511 or 332 (20 µg/ml) in the presence of collagen type IV (30 µg/ml). In these conditions, the RPE developed a significantly increased traction force compared to the one on 4kPa (~140 Pa for 511 and ~170 Pa for 332). This corresponded to a reduced efficiency of these monolayers for POS internalization (~ 40%) (Fig. 3 E - G). Second, we measured the phagocytic activity and traction forces of monolayers obtained on 4 kPa hydrogels coated with a high concentration of vitronectin (250 µg/ml) to match the protein surface density of laminins. Also in this case, the analyses revealed a higher average traction force (~ 200 Pa), which corresponded to a reduced ability of RPE to internalize POS (~ 36%) (Fig. 3 E – G).

To distinguish the exclusive role of cellular contractility from the possible converging effects of ECM signaling, we inhibited or increased actomyosin contractility in RPE monolayers using a ROCK inhibitor or a RhoA activator (Fig. 3 H - J). The reduction of contractility was performed on RPE monolayers cultured on soft (4 kPa) surfaces coated with collagen type IV (30 µg/ml) with little addition of laminins (2.5 µg/ml), which showed *per se* a low activity for POS phagocytosis (~ 50%). On the other hand, the increase of contractility was induced in RPE on high-density laminins (20 µg/ml) in the presence of collagen type IV. As expected, the drug treatments affected the ability of RPE to develop traction forces with reduced traction after ROCK inhibitor treatment and increased after RhoA activation (Fig. 3 H, J). Moreover, the quantification revealed a direct connection between actomyosin contractility and monolayer efficiency in POS phagocytosis. Independently of the laminin type, RPE phagocytic efficiency increased after ROCK inhibitor treatment (from ~50% to ~70%) and decreased after RhoA activator treatment (from ~70% to ~50%) (Fig. 3 H, J).

Overall, these data demonstrate that low laminin 511 and not 332 density reduces RPE functional capacity by promoting high levels of traction forces.

**Integrin β4/β1 ratio and keratin network organization modulate RPE mechanical homeostasis along the visual axis.**

Epithelial cells in homeostasis mechanically couple their cytoskeleton to their basement membrane laminins via integrin receptors (*5*, *44*). Intracellularly, integrin β1 subtypes interface with the actin cytoskeleton via talin, whereas integrin α6β4 binds via plectin the keratin network (*45*). Extracellularly, integrins β1 and β4 bind with a redundant number of proteins, including laminins α3 and α5 chains (*46*, *47*). Therefore, we wondered if low densities of laminin 332 or 511 differently promote integrin-based adhesion in RPE, thus influencing traction forces and consequent functional differences. Hence, we performed a functional adhesion assay using blocking antibodies to address the engagement of specific integrin subtypes on laminin-coated hydrogels (Fig. 4 A). Blocking the different beta chains (i.e., β1, β4, and [αv]β3) resulted in a significant reduction of adhesion for β1 (LN 511 ~62% and LN 332 ~75%) and no significant effect in the case of β4 and αvβ3 integrins. In the presence of integrin β4 blocking antibody, a tendency of reduction was observed on laminin 332. Hence, to avoid the effect of compensation by β1 integrin, we concurrently blocked integrin β1 and β4, achieving nearly complete inhibition of RPE cell adhesion onto low-density laminin 332 (~94%) with no significant drop on laminin 511 (Fig. 4 A, left). A similar trend was also observed for integrin alpha chains, where a substantial reduction in adhesion occurred upon combining integrin α6- and α3-blocking antibodies, suggesting the predominant involvement of these two subtypes in the adhesion process (Fig. 4 A, right).

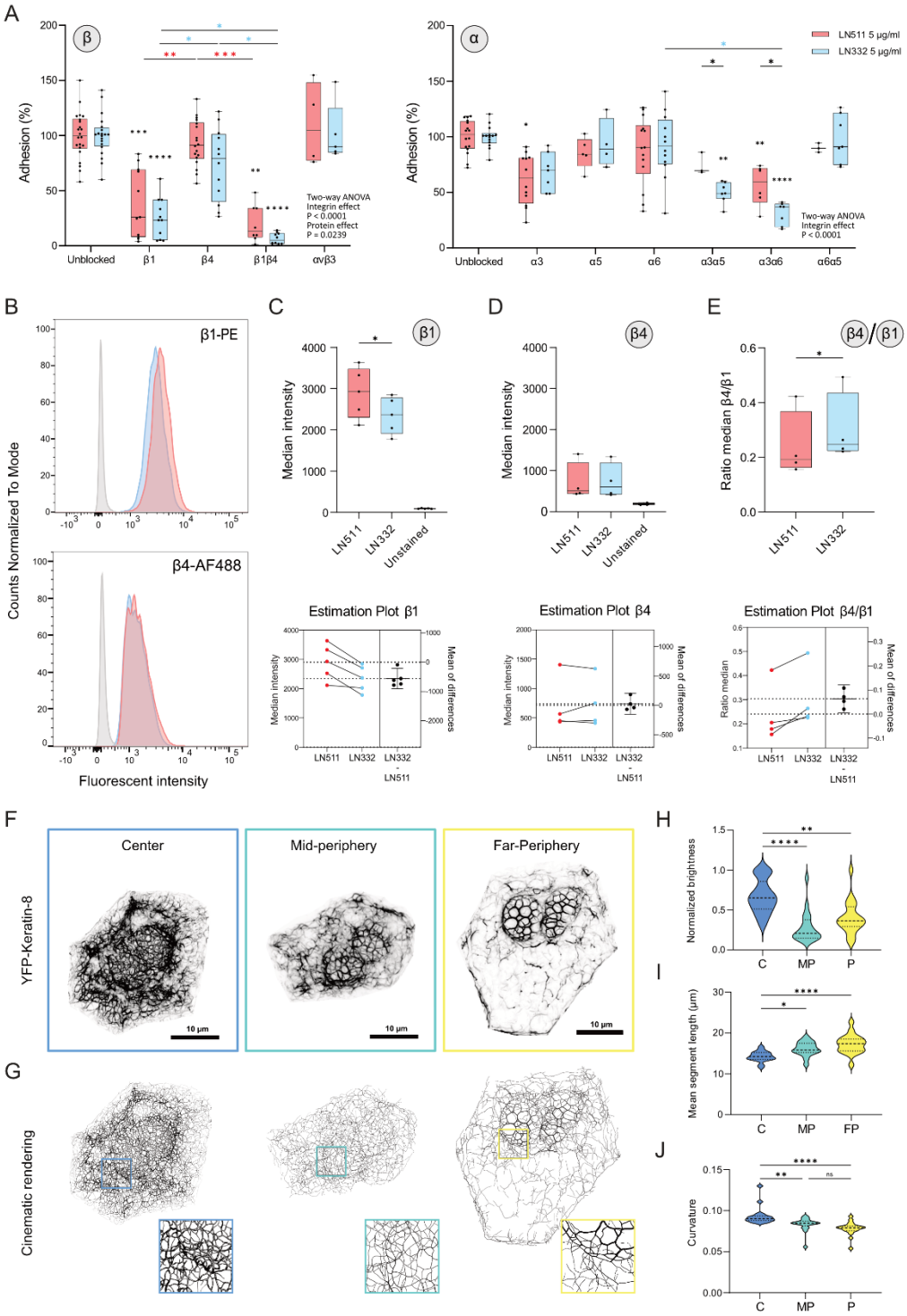


**Fig. 4. Laminin density defines RPE mechanical balance via integrin β4/β1 ratio and keratin cytoskeleton organization. (A)** Box and whisker plots of RPE cell adhesion percentage on low-density (5 µg/ml) laminin 332 or laminin 511-coated hydrogels, after incubation with integrin beta or alpha subunits blocking antibodies and control (cntr). * $p < 0.05$, ** $p < 0.01$, *** $p < 0.001$ ****$p<0.0001$ tested using a two-way ANOVA with Geisser-greenhouse and Tukey correction. Stars standing directly on the box and whisker show significance towards the control. **(B)** Representative flow cytometry histograms of the surface integrin β1 (top) and β4 (bottom) expression of RPE cell cultured for one week on low-density laminin 332 (light blue), laminin 511 (red), and unstained control (grey). **(C, D, E)** Box and whisker plots showing the distribution of intensity medians and the relative estimation plots from independent experiments for β1 and β4 integrins and their ratio. * $p < 0.05$ tested using paired t-test. **(F, G)** Representative images of RPE cells at different regions from YFP-keratin 8 mice and the resulting cinematic rendering of the keratin network. **(H, I, L)** Violin plots of normalized keratin brightness, mean segment length, and curvature in RPE from different retinal regions. * $p < 0.05$, ** $p < 0.01$ and ****$p<0.0001$ tested using a one-way ANOVA. Data are from three independent mice.

Based on these findings, we stained target integrins on RPE cells detached from mature monolayers and analyzed their relative surface presence during adhesion to the low-density laminin via flow cytometry (Fig. 4 B – E, sup. fig. 4). In line with the adhesion assay, the quantification revealed that cells adhering to the low-density laminin 511 present a significantly higher level of β1 integrin on their surface compared to cells adhering to laminin 332 (Fig. 4 B, C and supp. fig. 4 D). Instead, the levels of β4, α3 and α6 integrins were comparable between low-density laminin 511 and 332 (Fig. 4 D and sup. fig. 4 D - K). Furthermore, these results show that RPE cells adhering to low-density laminin 332 present a significantly higher ratio of integrin β4 to β1 compared to cells adhering to low-density laminin 511 (Fig. 4 E). Altogether, these data indicate the main role of integrins α6β1 and α3β1 to support the adhesion to the low-density laminin 511 and integrins α6β1, α3β1, and α6β4 to low-density laminin 332.

The presence of the hemidesmosomal integrin α6β4 has been shown to reduce cellular traction forces (*48*) and sensitivity of nuclear mechanotransduction (*49*) via their role in nucleation and organization of the keratin cytoskeleton (*49*, *50*). Encouraged by our *in vitro* findings, we were curious whether the different laminin densities in Bruch's membrane coincided with different organizations of the keratin network in RPE. Using keratin 8-YFP knock-in mice(*51*), we imaged and segmented the keratin network in 3D using a recently developed workflow (*52*) (Fig. 4 F - J). The analyses revealed that keratin network has thinner filaments (reduced brightness - fig. 4 H), higher segment length (Fig. 4 I), and reduced segments curvature (Fig. 4 J) from the center to far periphery.

This evidence supports the existence of a laminin-defined mechanical balance in RPE, which gradually shifts to a different keratin contribution in a more contractile monolayer toward the retinal periphery (Fig. 5).

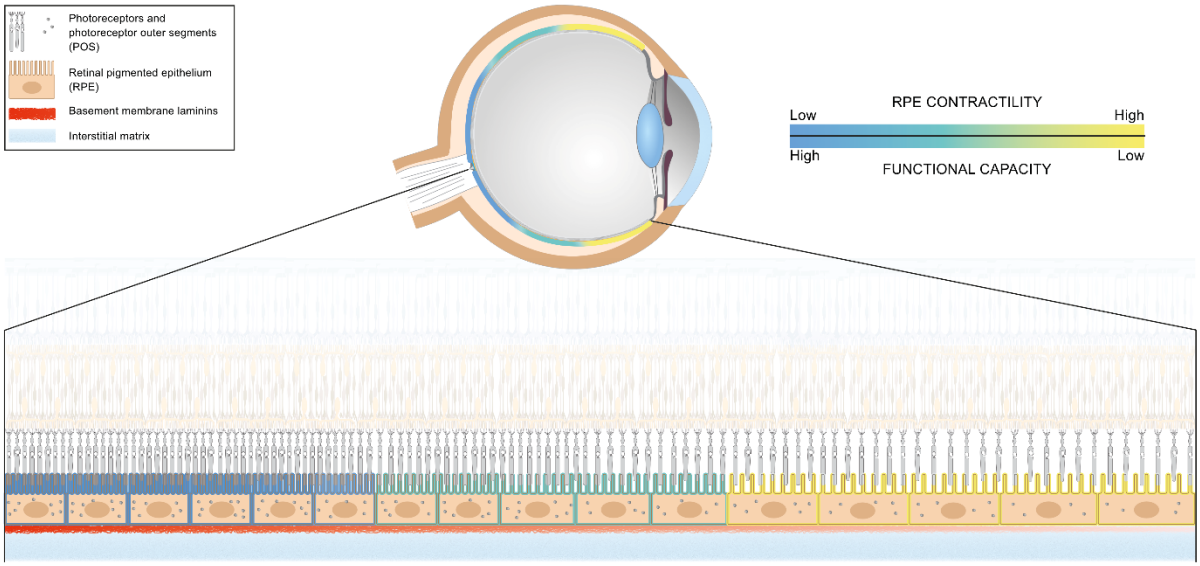


**Fig. 5. RPE mechanical homeostasis along the visual axis.** Schematics of ECM-orchestrated changes in the retinal tissue shows how high basement membrane laminin density in the macula ensures a mechanical status that supports maintaining high functional demand. Low laminin density in the retinal periphery increases RPE contractility, which correspond to diminished functional capacity.

## Discussion

Our findings demonstrate a direct role of laminin density in regulating RPE functional capacity through epithelial contractility. For the first time, we report the presence of a relative density gradient of specific laminin isoforms in the Bruch's membrane *in vivo*. The Bruch's membrane has the highest laminin content at the retinal center, whereas at the far periphery, the laminin 332 and α5-containing isoforms have the lowest density. This laminin density gradient correlates with a different topology and with a gradual increase in RPE cellular shape factor with the lower laminin density corresponding to more elongated cells. Cellular shape factor and cell-to-neighborhood relationship directly correspond to mechanical properties of the epithelial monolayers (*18–20*) and contractility (*21*, *37*, *38*). Finally, the different arrangements of the keratin network within the RPE imply that, towards the periphery, the actin cytoskeleton may have a more prominent contribution to the epithelial mechanical status. Altogether, this evidence strongly indicates higher epithelial contractility at the far periphery compared to the center.

Due to technical limitations for the direct *in vivo* quantification of mechanical properties and contractility, we employed a human-relevant *in vitro* model using hiPSC-derived RPE cells cultured on laminin-functionalized PAA gels. The stringent condition for ECM availability and remodeling, created by the PAA gel, revealed a direct role of low-density laminin 511 in increasing RPE contractility (higher traction forces and monolayer stress) and reducing the epithelium efficiency to phagocyte POS. Despite this increase in RPE contractility, there were no observed alterations in cell shape or topology. This suggests that the monolayer topology and morphology *in vivo* may be defined by the convergence of several factors, such as RPE's anchorage to the ora serrata at the retinal periphery (*53*). Moreover, our data rule out the exclusive role of laminins in defining RPE monolayer organization or stiffness.

The effect of laminin α5 on cellular mechanics is not surprising. Laminin α5-containing isoforms have been shown to enhance cell stiffness and support better shear stress mechanotransduction (*54*) and intercellular tightness (*55*) in the endothelium. As shown for the endothelium, RPE cells also preferentially adhere to this laminin by β1 integrins (i.e., α3β1 and α6β1 integrins). This is different from laminin 332, which additionally supports RPE adhesion via α6β4 integrins, i.e., hemidesmosomes. The role of hemidesmosomes in organizing the keratin network is crucial for the mechanical integrity of epithelial tissues (*56*, *57*) and was proposed to define their textile nature (*44*). More recently, data from different labs demonstrated that hemidesmosomes and the keratin network reduce cellular traction force (*48*) and protect the nucleus from mechanical strain (*49*). In agreement with the tensegrity model, cellular mechanics is a balance of cytoskeleton-driven forces, where a contractile actin cytoskeleton is counterbalanced by intermediate filaments (*58–60*). Therefore, a higher ratio of β4/β1 integrins in RPE adhering to low-density laminin 332 by the more prevalent presence of the hemidesmosomes could explain the quantified low traction forces in contrast with low-density laminin 511, which promotes higher epithelial traction. Similarly, a thinner and tenser keratin network in RPE in the far periphery and elongated nuclei suggest a higher contribution of the contractile actin cytoskeleton to tissue mechanics in this area. Nevertheless, technical challenges leave the open question of whether the relative amount of laminin isoforms differ along the visual axis and if the ratio between β4 integrins (hemidesmosomes) and β1 integrins decreases with the distance from the optic nerve.

The fact that ECM density reduction increases epithelial traction has been previously proposed based on the reduction of integrin β1 receptor engagement *in vitro* (*36*, *61*). Here, for the first time, we show the physiological relevance of this density and the importance of the β4/β1 ratio for epithelial mechanics. Future studies will need to focus on the molecular

mechanisms regulating epithelial mechanical homeostasis by laminin receptors' density. This is particularly relevant for retinal aging, given the reported reduction in hemidesmosomal attachment sites in RPE (*62*).

A study on stem cell-derived RPE has previously shown that the organization of the actin cytoskeleton can predict the ability of differentiated cells to phagocyte POS (*33*). Particularly, the presence of F-actin stress fibers impaired the phagocytic activity of these cells. These data and our findings strongly suggest that high contractility in RPE is detrimental to its homeostasis and function. RPE apical microvilli interact with POS mostly via the Mer tyrosine kinase receptor (MerTK) and the integrin αvβ5 (*63*). The activation of MerTK is thought to be involved in the inside-out activation of integrin αvβ5 with the recruitment of talin, vinculin and interaction with F-actin (*63*). These focal adhesion-like structures have already been shown to mediate phagocytosis in macrophages and to be mechanosensitive (*64*). Hence, the formation of this apical molecular clutch may be sensitive to the overall cellular contractility defined by the ECM substrate and explains the lower efficiency of POS internalization observed in this work. Furthermore, the homophilic interaction between POS and RPE via the neural cell adhesion molecule (N-CAM) may also be impacted by increased RPE contractility affecting the bond lifetime, thus, binding efficiency.

Overall, our work underlines the important role of RPE mechanobiology for outer retina physiology and opens important questions about its role in retinal aging. ECM remodeling while aging may affect cell adhesion and shift RPE mechanical homeostasis out of its optimal range, making it more prone to phenotypical changes. Overcoming this threshold may cause sight-impairing diseases such as (high) myopia and age-related macular degeneration. Moreover, the use of Rho kinase inhibitors, as in glaucoma treatment (*65*, *66*), may be implemented to prevent the progression of RPE-specific diseases. Undoubtedly, further studies will be necessary to elucidate to what extent RPE contractility is involved in outer retina diseases.

## Materials and Methods

**Retina flat mount preparation.** Retina flat mounts were prepared from BALB/c mice of 25-30 weeks of age. After sacrifice, the eyes were enucleated and fixed with 2% (wt/vol) paraformaldehyde (PFA) for 4 hours at 4°C rotating. To best visualize the RPE layer, the eyes were prepared as flat mounts according to published protocol(*67*). Briefly, the cornea, the iris and the lens were removed, and the eyecup was cut into eight longitudinal slices to allow its spreading. Afterwards, the neurosensory retina was gently detached exposing the RPE layer adhering to its ECM for fluorescent staining and imaging. The animal care and sacrifice were conducted according to the German Animal Welfare Act (LANUV, reference number 84- 02.04.2015.A190).

**Atomic force microscopy of Bruch's membrane.** Upon enucleation, murine eyes were freshly dissected using cold phosphate-buffered saline without $Ca^{2+}$ and $Mg^{2+}$ ($PBS^{-/-}$) and containing protease inhibitors as instructed by the manufacturer (Roche, 4693132001). Dissected eyes were denuded by the RPE layer via incubation of the tissue for 60 minutes with 50 mM Tris–HCl buffer plus 20 mM ethylenediamine tetraacetic acid (EDTA), pH 7.4, followed by 20 minutes incubation in 50 mM Tris–HCl buffer and two washes of 10 minutes with 1 M NaCl, pH 7.4. Each solution contained freshly added cOmplete™, EDTA-free Protease Inhibitor Cocktail (Roche, 4693132001). Next, the prepared eyes were glued to a surface using Corning Cell-Tak Cell and Tissue Adhesive (Corning, 354240). Cantilevers with a spherical colloidal tip of 6.62 µm diameter (Nano and More GmbH, CP-PNPS-SiO-C-5) were used to indent 200 nm into the decellularised Bruch's membrane in different

regions of the eye. The experiments were performed in a Dimension Icon atomic force microscope (Bruker Co. USA). Probes were calibrated using the thermal oscillation method, built into the software (Nanoscope 9.4). Force distance curves were recorded with an approach and retraction speed of 1 µm/s, with a relative maximal force set typically to 2 nN. The maximal range of the Z distance was set to 2.5 µm. All curves were exported to ASCII files with the analysis software of the instrument. The approach part of the curves was analyzed using a custom-written script in Python (https://www.python.org) using the Hertz model (equation (1)). The Poisson ratio was assumed to be $\nu = 0.3$. The last 40-50% of the data points are fit to a line and subtracted as background.

$$F(\delta) = \frac{4}{3}\frac{E}{1-\nu^2}\sqrt{R}(\delta - \delta_0)^{3/2} \qquad (1)$$

The model fits the whole curve using a nonlinear fit (leastsq) from Scipy (https://www.scipy.org) finding both Young's modulus and the contact point. (code is available under: https://github.com/tomio13/AFMforce).

**Immunofluorescence of retinal tissue.** Fluorescent staining of retina flat mounts was performed as follows. After fixation and dissection, the tissue was incubated for one hour in 1% bovine serum albumin (BSA) (wt/vol) in $PBS^{-/-}$ containing 0.1% (vol/vol) Triton X-100, followed by overnight staining at 4ºC with primary antibodies or phalloidin dissolved in $PBS^{-/-}$ solution of 1% (wt/vol) BSA and 0.1% (vol/vol) Triton X-100. Secondary antibodies were diluted in $PBS^{-/-}$-containing 0.1% (vol/vol) Triton X-100 and incubated with the tissue at room temperature for two hours. Finally, the retinas were incubated for 15 minutes with 5 µg/ml Hoechst 33342 (Thermo-Fischer Scientific, 62249) in $PBS^{-/-}$ before being mounted on glass slides with Mowiol mounting medium (Sigma-Aldrich). Primary and secondary antibodies used in this work are listed in supplementary table 1.

**Retinal extracellular matrix quantification.** To quantify the relative amount of ECM protein in the Bruch's membrane upon immunofluorescence staining, Z-stacks (0.5 µm optical slices) from the different regions were obtained using a Zeiss LSM 710 (Carl Zeiss) confocal microscope with a Plan-Apochromat 63 x/1.4-NA, DIC M27 oil immersion objective using unified illumination settings. The distance from the optic nerve was monitored using the automated stage of the microscope and setting the optic nerve as an origin. Within the eye, Z-stacks for each region were recorded per eight longitudinal slices, respectively. Mean fluorescent intensity in single optical sections identified as BrM was measured using Fiji software (National Institutes of Health, USA). Manually defined regions of interest (ROIs) were selected to avoid artefacts due to tissue tearing during preparation (Fig. 1 I "stars"). Three to five ROIs were measured for each stack, and the fluorescence intensity of all data was normalized to the highest measured value in the eye.

**Keratin-8 network segmentation and characterization.** Retinas for keratin-8 analysis were prepared as flat mounts from homozygous keratin 8-YFP knock-in mice (*51*). In each region (center, mid periphery and far periphery), z-stacks of six cells were recorded per animal using a Plan-Apochromat 63 x/1.4-NA, DIC M27 oil immersion objective in Airyscan mode at a Zeiss LSM 710 (Carl Zeiss), for a total of 54 analyzed cells. To ensure the analysis of only individual cells, the signal within individual cells was cropped from confluent monolayers using standard tools in Fiji. Cell borders were manually defined for each z-slice and the cell exterior was set to a grey value of 0. The obtained images were segmented and processed to obtain a keratin network model for each cell as previously

440 described (*52*) Finally, custom-made Matlab scripts were used to analyze the network
441 properties including brightness, segment length and curvature (*52*).
442
443 **hiPSC-RPE culture.** Differentiated hiPSC-RPE were purchased cryopreserved from
444 FUJIFILM Cellular Dynamics and after thawing, seeded in 24-well plates coated with 2.5
445 µg/ml Vitronectin XF (StemCell Technologies, 07180) at a density of 1600-1800 cells/mm$^2$.
446 Cells were cultured to confluence in a humidified incubator at 37°C and 5% $CO_2$ and then,
447 after detachment, reconstituted in CELLBANKER 2® freezing media (Amsbio LLC,
448 11891) and kept in liquid nitrogen for future use. Cell detachment for cryopreservation or
449 experiments was achieved through 30 minutes of incubation with 5 mM EDTA in PBS
450 without $Ca^{+2}$ and $Mg^{+2}$ ($PBS^{-/-}$) followed by TrypLE Express dissociation agent (Gibco,
451 12605-010) for five minutes at 37ºC. Prior to seeding, cells were centrifuged at 300 g for 5
452 minutes and resuspended in the media at the desired density. For the experiments, cells were
453 thawed again and cultured for up to two weeks until confluence before use. For seeding on
454 polyacrylamide hydrogels, cells were seeded at a density of 5000-6000 cells/mm$^2$,
455 corresponding to the RPE density in the human macula (*15*) and cultured for one week.
456 Cells were cultured in hiPSC-RPE medium composed of MEM α (Thermo Fisher, 12549-
457 089), 5% (vol/vol) knock-out serum replacement (Gibco, 10828-028), 1% (vol/vol) N-2
458 supplement (Gibco, 17502-048), 55 nM hydrocortisone (Sigma-Aldrich, H6909), 250
459 µg/ml taurine (Sigma, T0625), 14 pg/ml triiodo-L-thyronine (Sigma, T5516) and 25 µg/ml
460 gentamicin (Gibco, 15750-060). The medium was exchanged every second day.
461
462 **Hydrogel preparation and functionalization.** To obtain flat hydrogel substrates, a mixture
463 of 40% acrylamide (Bio-Rad, 1610140) and 2% bis-acrylamide (Bio-Rad, 1610142) in
464 distilled water was first prepared. The following ratios of acrylamide / bis-acrylamide in the
465 mixture were used to reach different hydrogel Young's moduli quantified by
466 nanoindentation: 5 % / 0.1 % (wt/vol) for 4 kPa and 10% / 0.07 % (wt /vol) for 18 kPa.
467 Then, the mixture was combined with 0.5 % of (vol/vol) ammonium persulfate (Sigma
468 Aldrich, 248614, 10 % (wt/vol) stock solution in distilled water) and 0.05 % (vol/vol) N`-
469 tetramethylethylenediamine (TEMED) (Sigma Aldrich, 411019), and pipetted between
470 glutaraldehyde-activated glass bottom petri dishes (Cellvis, D35-20-0-N) and a
471 hydrophobic glass coverslip. If hydrogels were used for traction force microscopy, 1 µm
472 yellow-green carboxylate-modified polystyrene microbeads (Sigma, L4655) were included
473 in the solution.
474 ECM proteins were crosslinked on the hydrogels' surface according to the protocol
475 described by Przybyla L. and colleagues (*34*). Briefly, for functionalization solution, we
476 prepared stocks of 0.5 M HEPES NaOH pH6 and 0.2% (wt/vol) bis-acrylamide in distilled
477 water, 0.2 % (vol/vol) tetramethacrylate (Sigma, 408360) and 3% (wt/vol) hydroxy-4′-(2-
478 hydroxyethoxy)-2-methylpropiophenone (Sigma, 410896) in ethanol. Acrylic acid N-
479 hydroxysuccinimide ester (Sigma, A8060) was initially dissolved in DMSO (10 mg/ml) and
480 later reconstituted in 50% ethanol for the final concentration of 0.03 % (wt/vol). Calculating
481 0.5 ml solution per gel, we combined 216.65 µl of sterile water, 50 µl of 0.5 M HEPES
482 NaOH pH 6, 32.5 µl of ethanol and 25 µl of bis-acrylamide and degassed under vacuum for
483 20 min. Then, 5 µl tetramethacrylate, 4.165 µl hydroxy-4′-(2-hydroxyethoxy)-2-
484 methylpropiophenone and 5 µl of the ester reconstituted in 161.65 µl of 50% ethanol were
485 added to the degassed solution. The completed functionalization solution was applied over
486 the surface of hydrogels, previously partly dehydrated in a 70% ethanol solution for
487 5 minutes, and the hydrogels were exposed for 10 minutes to ultraviolet light. After
488 sequential double washing with 25 mM HEPES buffer and $PBS^{-/-}$ for a total of 20 minutes,
489 the gel surface was incubated overnight at 4ºC with the desired ECM protein solution.

Human recombinant laminin-511 (Biolamina, LN511-0202) and laminin-332 (Biolamina, LN332-0202) were prepared at the desired concentration in PBS containing $Ca^{2+}$ and $Mg^{2+}$ ($PBS^{+/+}$) mixed with 30 µg/ml collagen type IV (Sigma-Aldrich, M7027-100G). Vitronectin (StemCell Technologies, 07180) was used without dilution at 250 µg/ml. Finally, the obtained hydrogels were washed in $PBS^{+/+}$ and sterilized by 30 min ultraviolet light irradiation before their application as cell culture substrates.
To represent surface protein saturation, gels were chemically crosslinked and coated with laminin-511 at concentrations of 5, 10, 20 or 30 µg/ml along with collagen type IV (30 µg/ml) in $PBS^{+/+}$. After overnight incubation at 4°C, gels were thoroughly washed with $PBS^{+/+}$ to remove unbound protein, fixed with 2% PFA for 10 minutes at room temperature, blocked with 1% BSA and stained with primary Anti-mouse laminin α5 (gift from Lydia Sorokin) and secondary Anti-mouse IgG AF594 (Invitrogen, A11005). Between all steps, gels were washed with $PBS^{-/-}$ for at least 1 h. Stained gels were imaged with a 63x objective on ApoTome.2 Fluorescence Microscope (Carl Zeiss), with at least 10 regions per gel. The average intensity of each image was measured using Fiji software, and the final results were plotted in GraphPad Prism 10.

**Immunofluorescence staining of hiPSC-RPE.** Cells on hydrogels were first quickly washed with warm (~37 ºC) $PBS^{+/+}$ then fixed with warm (~37 ºC) 2% (wt/vol) PFA for 8 minutes at room temperature. After fixation, cells were permeabilized with 0.3% (vol/vol) Triton X-100 for 2 minutes and blocked with 1% (wt/vol) BSA for 30 minutes at room temperature. Primary antibodies or Phalloidin-iFluor 647 Reagent (Abcam, ab176759) in PBS containing 1% (wt/vol) BSA were incubated overnight at 4ºC. The following day, secondary antibodies were diluted in a PBS solution containing DAPI (1 µg/ml, Invitrogen D1306) and incubated with the sample for 30 minutes at room temperature. Primary and secondary antibodies used in this work are listed in supplementary table 1. The samples were imaged in PBS solution to match the immersion type of the objective. Cells were imaged using Plan-Apochromat 40x water immersion objective on Zeiss LSM 710 confocal microscope with Airyscan capability (Carl Zeiss).

**Live staining.** For live imaging of F-actin, hiPSC-RPE cells cultured on PAA gels were incubated with 500 nM of a fluorogenic F-actin probe SirActin (Spirochrome, SC001) containing medium for at least two hours before imaging. The samples were imaged using Plan-Apochromat 40x water immersion objective on Zeiss LSM 710 confocal microscope with Airyscan capability (Carl Zeiss). Orthogonal views from Z-stacks acquired via confocal live-imaging of F-actin (SirActin) were used to measure the average junctional height of cultured RPE monolayers using Fiji image processing package (National Institutes of Health, USA).

**Morphometric and topology analyses.** Microscopy images of RPE *in vivo* and *in vitro* were segmented using the cellpose software (*68*) (www.cellpose.org) applied on F-Actin micrographs. Segmented cells were imported into Fiji as ROIs and used to generate skeletonized images. The skeletonized images were then imported into custom-written MATLAB software (*69*). Prior to analysis, the software removes 15 pixels on the sides of the images to remove poor mask definition by cellpose (Sup. fig. 1 B), and then applies a Gaussian filter with a standard deviation of 2 pixels (function "imgaussfilt") to correct the pixel connectivity on the masks provided by cellpose. Finally, the software extracts information about the cell morphology (cell area, perimeter, and elongation) and topology (cell neighbors) as previously described (*69*). For these analyses, the cells at the edge of the picture were not considered to avoid any segmentation error (Sup. fig. 1 C). For *in vivo*

images, in total, 24 images from 3 different mice have been analyzed for the "center" and "mid periphery" regions of the retina (8 images each) and 23 images for the "far periphery" region (8-8-7 images for the 3 mice respectively). This corresponds to a total cell number of 5575 cells for the center, 7957 for the mid periphery and 7863 for the far periphery. For *in vitro* images, 71 images were analyzed (at least 2 images per experiment). Each image provided in between 86 and 312 cells. Because of segmentation error, to remove unnaturally large cells, cells with a rescaled area (see below) higher than 2, and cells with a neighborhood larger than 10 cells have been removed from the analysis. The number of cells per condition is summarized in supplementary table 2. To build both Lewis' and Desh' law, data were separated with respect to their number of neighbors and binned in different classes before being averaged. To build Aboav-Weaire's law, the cells at the images' edge were removed, since their neighborhood is not defined. For that, the neighborhood of each cell is reconstructed to determine the average position of the collection of neighbors. If the distance between their average position and the central cells is less than 30 px, the central cell is assumed to be in the bulk of the image and not on the border of the image. To plot Aboav-Weaire's law, we computed b(n) defined in (2).

$$b(n) = (n-6)\mu_{m(n)} - \sigma_n^2 \qquad (2)$$

where $\mu_{m(n)}$ is the mean size of the neighborhood among the neighbors, and $\sigma_n^2$ is the central second moment of the distribution of neighbours, i.e., its variance. Such distribution is taken for a given mouse, not among different mice. Data from the different mice are average together with a ponderation proportional to the total number of cells making the statistics.

**Scanning Electron Microscopy** (Critical Point Drying). After a week in culture on a polyacrylamide gel with the defined coating, hiPSC-RPE were fixed in 3% glutaraldehyde (Agar scientific, Wetzlar, Germany) for 4 h at 4°C followed by a washing in 0.1 M Soerensen's Phosphate Buffer (Merck, Darmstadt, Germany). The dehydrating step was performed in the ascending alcohol series with 10 minutes duration each. The samples were sequentially immersed in the following solutions: 30% ethanol, 50% ethanol, 70% ethanol, 90% ethanol, and three times in 100% ethanol. Critical Point Drying was performed in liquid CO2. Prior to imaging, cell monolayers were coated with 10 nm gold/palladium layer.

**Proliferation assay.** Levels of proliferation in hiPSC-RPE monolayers were assessed using a proliferation assay kit Click-iT EdU (Thermo Fisher, C10337). Cells were incubated with a 1:1 mixture of cell culture supernatant and 5-Ethinyl-2'-Desoxyuridin (EdU) (20 µM) containing hiPSC-RPE cell culture medium for 24 h. Final EdU concentration in the mixture was 10 µM. Afterwards, cells were fixed as described for immunofluorescent labelling and processed according to the manufacturer's instructions. As EdU incorporates into newly synthesized DNA, proliferating cells were identified as having their nucleus positively stained with EdU-Alexa Fluor 488. The total area of the gel was imaged on Axio Observer 7 (Carl Zeiss) microscope as an overview using the tiles option. The ratio of proliferating cells was calculated in comparison with DAPI-positive nuclei and quantified using the particle analysis plugin of Fiji software (National Institutes of Health, USA).

**Photoreceptor outer segment internalization assay**. Photoreceptor outer segments (POS) were isolated in batches from porcine eyes from a local slaughterhouse as previously described (*70*). Briefly, the eyes were dissected using a red safelight lamp as the only illumination source, and the neural retina was collected. After retinal mechanical homogenization, POS were isolated via ultracentrifugation in a sucrose gradient. Thereafter, POS were labelled with 2.5 mg/ml FITC dye (Thermo Fisher, F1906), resuspended in DMEM (Thermo Fisher, 31331-028 ) containing 2.5% sucrose and stored in aliquots at -80

ºC for future use. For internalization assay, POS aliquots were thawed in a water bath, washed with medium, centrifuged at 2300g for 5 min and resuspended in hiPSC-RPE cell medium to an amount of roughly 10 POS per RPE cell in culture. Human MGF-E8 protein (R&D Systems, 2767-MF-050) and human protein-S (Coachrom, pp012A) were added at respectively 2.4 µg/ml and 2 µg/ml to aid the internalization. Next, hiPSC-RPE monolayers were washed twice with warm media and incubated for four hours at 37°C with the prepared mixture at a density of approximately ten POS per cell. After incubation, the monolayers were gently washed four times with warm $PBS^{+/+}$ and fixed for fluorescence staining as described. Phagocytosis efficiency was calculated as projected area of internalized POS divided by the total projected POS area in the same field of view. Internalized POS were identified in orthogonal views from confocal optical sections (0.5 µm) by using F-actin staining to distinguish between apical-bound and internalized segments. Analyses were automatized with the particle analyses plugin of Fiji software (National Institutes of Health, USA) after applying a binary mask on the images.

**Traction force and monolayer stress microscopy.** Traction force quantification and monolayer stress calculations were performed as previously described (*36*, *37*). Briefly, a week-old monolayer cultured on a PAA gel substrate containing fluorescent beads was imaged using Axio Observer 7 (Carl Zeiss) microscope for the beads signal. Then, the monolayer was detached with 0.5% SDS solution in $PBS^{-/-}$ followed by washing steps and 20 minutes of gel incubation in cell media to prevent gel shrinkage due to the solvent change. The positions of the fluorescent beads in the hydrogel after the cell detachment (relaxed state of the gel) were compared with the tense gel before, and beads displacement vectors were calculated using the particle image velocimetry (PIV) plugin of Fiji (National Institutes of Health, USA). Traction forces were calculated from these vectors using the Fourier transform traction cytometry plugin (FTTC) of Fiji (National Institutes of Health, USA). Next, based on the traction force information, average normal stress vectors were calculated using a force balance algorithm in MATLAB (MathWorks) as formulated elsewhere (*36*, *37*). For each measured sample, the average cell height was calculated using a live actin staining (SirActin, Spirochrome) to correctly input the force balance algorithm.

**Stiffness measurements of hiPSC-RPE monolayers.** Measurements were performed using a Chiaro Nanoindenter System (Optics 11 Life) mounted on Zeiss Axio Observer 7 (Carl Zeiss) with an environmental chamber sustaining 37°C. A probe of 10 µm radius and 0.025 N/m stiffness (Optics 11 Life) was used and the indentation was performed in Displacement control mode, indenting 10 µm into the cell monolayer. Approach curves were fitted via the DataViewer V2.4.0 software (Optics 11 Life) using a Hertzian contact model according to a set indentation depth from 0 to 3 µm for the apical stiffness. A Poisson's ratio of 0.5 was used and a maximum load of 30% was allowed for setting the contact point. Only results from well fitted data ($R^2 > 0.95$) were considered for statistics.

**Drug experiments.** For activation of the RhoA-dependent pathways, we incubated RPE monolayers with Rho activator II (Cytoskeleton, CN03-A) and Rho kinase (ROCK) inhibitor Y-27632 (Sigma Aldrich, Y0503)(*71*). Briefly, the one-week-old RPE monolayers on a hydrogel coated with high laminin density (20 µg/ml) were treated with Rho activator II (1 µg/ml) containing media for 3 hours prior to POS phagocytosis assay or traction force measurements to promote the actomyosin contractility, or with an equal volume of water as a solvent control. To reduce the actomyosin contractility at low laminin surface density (2.5 µg/ml), ROCK inhibitor (25 µM) was added to the media one hour prior the POS

phagocytosis assay or traction force measurements. An equal volume of DMSO was used as a solvent control. Further analysis was performed as described in the relevant chapters.

**Adhesion assay.** For cell adhesion assay, a confluent monolayer of hiPSC-RPE cells cultured in a 24-well plate was detached with 30 minutes incubation of 750µl of 5 mM EDTA in $PBS^{-/-}$ without enzymatic treatment to prevent unwanted receptor cleavage. Cells were gently washed with an additional 750 µl of EDTA in $PBS^{-/-}$ and the whole solution was transferred into the 15 ml Falcon tube. After cell counting, the suspension was centrifuged at 300 g for 5 minutes. The pellet was resuspended in ice-cold media in half the volume required for the experiment and transferred to low protein binding tubes. Ice-cold media should contain 20 µg/ml blocking antibody for blocking experiments. After 15 minutes of incubation on ice, the cell suspension was diluted (1:2) with the equivalent volume of warm media and immediately transferred onto the hydrogel surface. After 15 minutes at 37°C and 5% $CO_2$, hydrogel surfaces were gently washed with warm $PBS^{+/+}$ to remove not attached cells, fixed with 2% PFA at room temperature for 8 minutes, and stained for F-Actin (Phalloidin-iFluor 488 Reagent, Abcam - ab176753) for analysis. The number of attached cells was quantified using the particle analysis plugin in Fiji software and normalized to the mean of control samples to convert as a percentage of adhesion. The following azide-free blocking antibodies were used: integrin β1 (clone P5D2) (Santa Cruz, sc-13590 L), integrin β4 (clone ASC-8) (Merk, MAB2059Z), integrin αvβ3 (clone LM609) (Merk, MAB1976Z), integrin α3 (clone P1B5) (Merk, MAB1952Z), integrin α5 (clone P1D6) (Merk, MAB1956Z), integrin α6 (clone GOH3) (Santa Cruz, sc-19622 L).

**Flow cytometry.** One-week-old hiPSC-RPE cells were carefully detached from the hydrogel substrate by incubation with 10 mM EDTA in $PBS^{-/-}$ at 37°C and 5% $CO_2$ for 30 minutes, followed by Accutase solution (Sigma Aldrich, A6964) for 15 minutes. During this period, gentle shaking was beneficial for detachment. Cells were gently washed from the surface with an additional 1 ml of EDTA in $PBS^{-/-}$, transferred into the 15 ml tube and centrifuged for 5 minutes at 300 g. After centrifugation, cells were dispersed in ice-cold $PBS^{-/-}$ and divided into two separate tubes: one will contain the whole antibody panel, and another will be stained for β4 integrin alone. For the first tube, the viability staining with LIVE/DEAD™ Fixable Near IR(780) Viability Kit (Thermo Fisher Scientific, L34992) was performed during the 15-minute incubation on ice protected from the light. After centrifugation at 300 g for 4 minutes, cells were fixed with 1 ml of 1% PFA for 5 minutes on ice and resuspended in 100 µl of $PBS^{-/-}$ containing 3% BSA and 5 mM EDTA (FACS buffer) for 6 minutes centrifugation at 300 g. Fluorescently conjugated antibodies (see table 1) were added according to the manufacturer's instructions and incubated with cells for 45 minutes on ice protected from the light. After washing, cells were resuspended in 400 µl of the FACS buffer and filtered using the Flowmi(R) Cell Strainer (MERK, BAH136800040) directly into the flow cytometry tube for the measurements. Stained cells were analyzed using a BD LSRFortessa flow cytometer equipped with 405, 488, 561 and 640 nm lasers. Analysis of the data was carried out using the FlowJo software.

**Statistics.** Statistical analysis was performed using Prism (GraphPad). Data were tested for normality before proceeding to further statistical analyses. Sample conditions and the specific test used for each data set are indicated in corresponding figure captions.

689 **References**
690


691 1. A. A. Anlaş, C. M. Nelson, Tissue mechanics regulates form, function, and dysfunction.
692 *Curr Opin Cell Biol* **54**, 98–105 (2018).

693 2. N. M. E. Ayad, S. Kaushik, V. M. Weaver, Tissue mechanics, an important regulator of
694 development and disease. *Philosophical Transactions Royal Soc B* **374**, 20180215 (2019).

695 3. J. F. Eichinger, L. J. Haeusel, D. Paukner, R. C. Aydin, J. D. Humphrey, C. J. Cyron,
696 Mechanical homeostasis in tissue equivalents: a review. *Biomech Model Mechan* **20**, 833–
697 850 (2021).

698 4. J. D. Humphrey, E. R. Dufresne, M. A. Schwartz, Mechanotransduction and extracellular
699 matrix homeostasis. *Nat Rev Mol Cell Biology* **15**, 802–12 (2014).

700 5. A. N. Kozyrina, T. Piskova, J. Di Russo, Mechanobiology of Epithelia From the
701 Perspective of Extracellular Matrix Heterogeneity. *Frontiers Bioeng Biotechnology* **8**,
702 596599 (2020).

703 6. J. C. Booij, D. C. Baas, J. Beisekeeva, T. G. M. F. Gorgels, A. A. B. Bergen, The dynamic
704 nature of Bruch's membrane. *Prog Retin Eye Res* **29**, 1–18 (2010).

705 7. S. M. Raymond, I. J. Jackson, The retinal pigmented epithelium is required for
706 development and maintenance of the mouse neural retina. *Curr Biol* **5**, 1286–1295 (1995).

707 8. O. German, E. Buzzi, N. Rotstein, E. Rodriguez-Boulan, L. Politi, Retinal pigment
708 epithelial cells promote spatial reorganization and differentiation of retina photoreceptors. *J*
709 *Neurosci Res* **86**, 3503–3514 (2008).

710 9. D. Bok, The retinal pigment epithelium: a versatile partner in vision. *J Cell Sci* **1993**, 189–
711 195 (1993).

712 10. O. Strauss, The Retinal Pigment Epithelium in Visual Function. *Physiol Rev* **85**, 845–881
713 (2005).

714 11. A. Lakkaraju, A. Umapathy, L. X. Tan, L. Daniele, N. J. Philp, K. Boesze-Battaglia, D. S.
715 Williams, The Cell Biology of the Retinal Pigment Epithelium. *Prog Retin Eye Res* **78**,
716 100846 (2020).

717 12. R. W. Young, D. Bok, Partecipation of the Retinal Pigment Epithelium in the Rod Outer
718 Segment Renewal Process. *J Cell Biology* **42**, 392–403 (1969).

719 13. G. Wald, P. K. Brown, Synthesis and Bleaching of Rhodopsin. *Nature* **177**, 174–176
720 (1956).

721 14. S. Volland, J. Esteve-Rudd, J. Hoo, C. Yee, D. S. Williams, A Comparison of Some
722 Organizational Characteristics of the Mouse Central Retina and the Human Macula. *Plos One*
723 **10**, e0125631 (2015).

15. S. K. Bhatia, A. Rashid, M. A. Chrenek, Q. Zhang, B. B. Bruce, M. Klein, J. H. Boatright, Y. Jiang, H. E. Grossniklaus, J. M. Nickerson, Analysis of RPE morphometry in human eyes. *Mol Vis* **22**, 898–916 (2016).

16. Y.-K. Kim, H. Yu, V. R. Summers, K. J. Donaldson, S. Ferdous, D. Shelton, N. Zhang, M. A. Chrenek, Y. Jiang, H. E. Grossniklaus, J. H. Boatright, J. Kong, J. M. Nickerson, Morphometric Analysis of Retinal Pigment Epithelial Cells From C57BL/6J Mice During Aging. *Invest Ophth Vis Sci* **62**, 32 (2021).

17. D. Ortolan, R. Sharma, A. Volkov, A. Maminishkis, N. A. Hotaling, L. A. Huryn, C. Cukras, S. D. Marco, S. Bisti, K. Bharti, Single-cell–resolution map of human retinal pigment epithelium helps discover subpopulations with differential disease sensitivity. *Proc. Natl. Acad. Sci.* **119**, e2117553119 (2022).

18. E. Hannezo, J. Prost, J.-F. Joanny, Theory of epithelial sheet morphology in three dimensions. *Proc National Acad Sci* **111**, 27–32 (2014).

19. S. Alt, P. Ganguly, G. Salbreux, Vertex models: from cell mechanics to tissue morphogenesis. *Philosophical Transactions Royal Soc B Biological Sci* **372**, 20150520 (2017).

20. S. Kaliman, M. Hubert, C. Wollnik, L. Nuić, D. Vurnek, S. Gehrer, J. Lovrić, D. Dudziak, F. Rehfeldt, A.-S. Smith, Mechanical Regulation of Epithelial Tissue Homeostasis. *Phys Rev X* **11**, 031029 (2021).

21. D. Bi, J. H. Lopez, J. M. Schwarz, M. L. Manning, A density-independent rigidity transition in biological tissues. *Nat Phys* **11**, 1074–1079 (2015).

22. F. T. Lewis, A comparison between the mosaic of polygons in a film of artificial emulsion and the pattern of simple epithelium in surface view (cucumber epidermis and human amnion). *Anat Rec* **50**, 235–265 (1931).

23. F. T. Lewis, The correlation between cell division and the shapes and sizes of prismatic cells in the epidermis of cucumis. *Anat Rec* **38**, 341–376 (1928).

24. S. N. Chiu, Aboav-Weaire's and Lewis' laws—A review. *Mater Charact* **34**, 149–165 (1995).

25. S. Kim, M. Cai, S. Hilgenfeldt, Lewis' law revisited: the role of anisotropy in size–topology correlations. *New J Phys* **16**, 015024 (2014).

26. N. Rivier, Statistical crystallography Structure of random cellular networks. *Philosophical Mag Part B* **52**, 795–819 (2006).

27. D. A. Aboav, The arrangement of cells in a net. *Metallography* **13**, 43–58 (1980).

28. D. A. Aboav, The arrangement of grains in a polycrystal. *Metallography* **3**, 383–390 (1970).

759 29. D. Weaire, Some remarks on the arrangement of grains in a polycrystal. *Metallography* **7**,
760 157–160 (1974).

761 30. N. H. V. Chong, J. Keonin, P. J. Luthert, C. I. Frennesson, D. M. Weingeist, R. L. Wolf,
762 R. F. Mullins, G. S. Hageman, Decreased Thickness and Integrity of the Macular Elastic
763 Layer of Bruch's Membrane Correspond to the Distribution of Lesions Associated with Age-
764 Related Macular Degeneration. *Am J Pathology* **166**, 241–251 (2005).

765 31. D. A. Newsome, W. Huh, W. R. Green, Bruch's membrane age-related changes vary by
766 region. *Curr Eye Res* **6**, 1211–1221 (1987).

767 32. M. J. Song, R. Quinn, E. Nguyen, C. Hampton, R. Sharma, T. S. Park, C. Koster, T. Voss,
768 C. Tristan, C. Weber, A. Singh, R. Dejene, D. Bose, Y.-C. Chen, P. Derr, K. Derr, S.
769 Michael, F. Barone, G. Chen, M. Boehm, A. Maminishkis, I. Singec, M. Ferrer, K. Bharti,
770 Bioprinted 3D outer retina barrier uncovers RPE-dependent choroidal phenotype in advanced
771 macular degeneration. *Nat Methods* **20**, 149–161 (2023).

772 33. C. Müller, C. Charniga, S. Temple, S. C. Finnemann, Quantified F-Actin Morphology Is
773 Predictive of Phagocytic Capacity of Stem Cell-Derived Retinal Pigment Epithelium. *Stem*
774 *Cell Rep* **10**, 1075–1087 (2018).

775 34. L. Przybyla, J. N. Lakins, R. Sunyer, X. Trepat, V. M. Weaver, Monitoring
776 developmental force distributions in reconstituted embryonic epithelia. *Methods* **94**, 101–113
777 (2016).

778 35. M. Funaki, P. A. Janmey, Biology and Engineering of Stem Cell Niches. *Part Iii Des*
779 *Smart Biomaterials Mimic Control Stem Cell Niche*, 363–373 (2017).

780 36. J. Di Russo, J. L. Young, J. W. Wegner, T. Steins, H. Kessler, J. P. Spatz, Integrin α5β1
781 nano-presentation regulates collective keratinocyte migration independent of substrate
782 rigidity. *Elife* **10**, e69861 (2021).

783 37. M. Vishwakarma, J. Di Russo, D. Probst, U. S. Schwarz, T. Das, J. P. Spatz, Mechanical
784 interactions among followers determine the emergence of leaders in migrating epithelial cell
785 collectives. *Nat Commun* **9**, 3469 (2018).

786 38. J.-A. A. Park, J. H. Kim, D. Bi, J. A. Mitchel, N. T. Qazvini, K. Tantisira, C. Y. Park, M.
787 McGill, S.-H. H. Kim, B. Gweon, J. Notbohm, R. Steward, S. Burger, R, S. H. ell, A. T. Kho,
788 D. T. Tambe, C. Hardin, S. A. Shore, E. Israel, D. A. Weitz, D. J. Tschumperlin, E. P.
789 Henske, S. T. Weiss, M. Manning, J. P. Butler, J. M. Drazen, J. J. Fredberg, Unjamming and
790 cell shape in the asthmatic airway~epithelium. *Nat Mater* **14**, 1040–8 (2015).

791 39. C. Malinverno, S. Corallino, F. Giavazzi, M. Bergert, Q. Li, M. Leoni, A. Disanza, E.
792 Frittoli, A. Oldani, a, E. Martini, T. Lendenmann, G. Deflorian, G. V. Beznoussenko, D.
793 Poulikakos, K. Ong, M. Uroz, X. Trepat, D. Parazzoli, P. Maiuri, W. Yu, A. Ferrari, R.
794 Cerbino, G. Scita, Endocytic reawakening of motility in jammed epithelia. *Nat Mater* **16**, 587
795 (2017).

796 40. A. Palamidessi, C. Malinverno, E. Frittoli, S. Corallino, E. Barbieri, S. Sigismund, G. V.
797 Beznoussenko, E. Martini, M. Garre, I. Ferrara, C. Tripodo, F. Ascione, E. A. Cavalcanti-

Adam, Q. Li, P. P. D. Fiore, D. Parazzoli, F. Giavazzi, R. Cerbino, G. Scita, Unjamming overcomes kinetic and proliferation arrest in terminally differentiated cells and promotes collective motility of carcinoma. *Nat Mater* **18**, 1252–1263 (2019).

41. H. E. Balcioglu, L. Balasubramaniam, T. V. Stirbat, B. L. Doss, M.-A. Fardin, R.-M. Mège, B. Ladoux, A subtle relationship between substrate stiffness and collective migration of cell clusters. *Soft Matter* **16**, 1825–1839 (2020).

42. A. Mongera, ro, P. Rowghanian, H. J. Gustafson, E. Shelton, D. A. Kealhofer, E. K. Carn, F. Serwane, A. A. Lucio, J. Giammona, O. Campas, A fluid-to-solid jamming transition underlies vertebrate body axis elongation. *Nature*, doi: 10.1038/s41586-018-0479-2 (2018).

43. C. Pérez-González, G. Ceada, F. Greco, M. Matejčić, M. Gómez-González, N. Castro, A. Menendez, S. Kale, D. Krndija, A. G. Clark, V. R. Gannavarapu, A. Álvarez-Varela, P. Roca-Cusachs, E. Batlle, D. M. Vignjevic, M. Arroyo, X. Trepat, Mechanical compartmentalization of the intestinal organoid enables crypt folding and collective cell migration. *Nat Cell Biol*, 1–13 (2021).

44. J. Di Russo, T. M. Magin, R. E. Leube, A keratin code defines the textile nature of epithelial tissue architecture. *Curr. Opin. Cell Biol.* **85**, 102236 (2023).

45. B. Alberts, A. Johnson, J. Lewis, D. Morgan, M. Raff, K. Roberts, P. Walter, Molecular Biology of the Cell. 43–108 (2017).

46. M. Aumailley, The laminin family. *Cell Adhes Migr* **7**, 48–55 (2012).

47. R. O. Hynes, Integrins Bidirectional, Allosteric Signaling Machines. *Cell* **110**, 673–687 (2002).

48. W. Wang, A. Zuidema, L. te Molder, L. Nahidiazar, L. Hoekman, T. Schmidt, S. Coppola, A. Sonnenberg, Hemidesmosomes modulate force generation via focal adhesions. *J Cell Biol* **219**, e201904137 (2020).

49. Z. Kechagia, P. Sáez, M. Gómez-González, B. Canales, S. Viswanadha, M. Zamarbide, I. Andreu, T. Koorman, A. E. M. Beedle, A. Elosegui-Artola, P. W. B. Derksen, X. Trepat, M. Arroyo, P. Roca-Cusachs, The laminin–keratin link shields the nucleus from mechanical deformation and signalling. *Nat. Mater.*, 1–12 (2023).

50. M. Moch, R. E. Leube, Hemidesmosome-Related Keratin Filament Bundling and Nucleation. *Int. J. Mol. Sci.* **22**, 2130 (2021).

51. N. Schwarz, R. Windoffer, T. Magin, R. Leube, Dissection of keratin network formation, turnover and reorganization in living murine embryos. *Sci Rep-uk* **5**, 9007 (2015).

52. R. Windoffer, N. Schwarz, S. Yoon, T. Piskova, M. Scholkemper, J. Stegmaier, A. Bönsch, J. Di Russo, R. E. Leube, Quantitative mapping of keratin networks in 3D. *Elife* **11**, e75894 (2022).

53. L. Nobeschi, E. Freymuller, R. L. Smith, Intercellular Junctions in Rabbit Eye Ora Serrata. *Anatomia Histologia Embryologia* **35**, 287–292 (2006).

835 54. J. Di Russo, A. Luik, L. Yousif, S. Budny, H. Oberleithner, V. Hofschröer, J. Klingauf, E.
836 Bavel, E. N. Bakker, P. Hellstrand, A. Bhattachariya, S. Albinsson, F. Pincet, R. Hallmann,
837 L. M. Sorokin, Endothelial basement membrane laminin 511 is essential for shear stress
838 response. *Embo J* **36**, 183–201 (2016).

839 55. J. Song, X. Zhang, K. Buscher, Y. Wang, H. Wang, J. Di Russo, L. Li, S. Lutke-Enking,
840 A. Zarbock, er, A. Stadtmann, P. Striewski, B. Wirth, I. Kuzmanov, H. Wiendl, D. Schulte,
841 D. Vestweber, L. Sorokin, Endothelial Basement Membrane Laminin 511 Contributes to
842 Endothelial Junctional Tightness and Thereby Inhibits Leukocyte Transmigration. *Cell*
843 *Reports* **18**, 1256–1269 (2017).

844 56. B.-S. Hahn, M. Labouesse, Tissue integrity: Hemidesmosomes and resistance to stress.
845 *Curr Biol* **11**, R858–R861 (2001).

846 57. V. Todorović, K. R. Kligys, R. L. Dusek, J. C. R. Jones, K. J. Green, Encyclopedia of
847 Biological Chemistry (Second Edition). *Cell Archit Funct Article Titles D*, 636–643 (2013).

848 58. J. A. Broussard, A. Jaiganesh, H. Zarkoob, D. E. Conway, A. R. Dunn, H. D. Espinosa, P.
849 A. Janmey, K. J. Green, Scaling up single-cell mechanics to multicellular tissues – the role of
850 the intermediate filament–desmosome network. *J Cell Sci* **133**, jcs228031 (2020).

851 59. D. E. Ingber, N. Wang, D. Stamenović, Tensegrity, cellular biophysics, and the
852 mechanics of living systems. *Rep Prog Phys* **77**, 046603 (2014).

853 60. U. Rölleke, P. Kumari, R. Meyer, S. Köster, The unique biomechanics of intermediate
854 filaments – From single filaments to cells and tissues. *Curr. Opin. Cell Biol.* **85**, 102263
855 (2023).

856 61. R. Oria, T. Wiegand, J. Escribano, A. Elosegui-Artola, J. J. Uriarte, C. Moreno-Pulido, I.
857 Platzman, P. Delcanale, L. Albertazzi, D. Navajas, X. Trepat, J. M. García-Aznar, E. A.
858 Cavalcanti-Adam, P. Roca-Cusachs, Force loading explains spatial sensing of ligands by
859 cells. *Nature* **552**, 219–224 (2017).

860 62. R. E. Anderson, M. M. L. Vail, J. G. Hollyfield, Degenerative Diseases of the Retina. **1**
861 (1995).

862 63. W. Kwon, S. A. Freeman, Phagocytosis by the Retinal Pigment Epithelium: Recognition,
863 Resolution, Recycling. *Front Immunol* **11**, 604205 (2020).

864 64. V. Jaumouillé, A. X. Cartagena-Rivera, C. M. Waterman, Coupling of β2 integrins to
865 actin by a mechanosensitive molecular clutch drives complement receptor-mediated
866 phagocytosis. *Nat Cell Biol* **21**, 1357–1369 (2019).

867 65. G. Al-Humimat, I. Marashdeh, D. Daradkeh, K. Kooner, Investigational Rho Kinase
868 Inhibitors for the Treatment of Glaucoma. *J. Exp. Pharmacol.* **13**, 197–212 (2021).

869 66. K. J. Mandell, M. R. Kudelka, B. Wirostko, Rho kinase inhibitors for treatment of
870 glaucoma. *Expert Rev. Ophthalmol.* **6**, 611–622 (2011).

871 67. A. Claybon, A. J. R. Bishop, Dissection of a Mouse Eye for a Whole Mount of the
872 Retinal Pigment Epithelium. *J Vis Exp*, doi: 10.3791/2563 (2011).

873 68. C. Stringer, T. Wang, M. Michaelos, M. Pachitariu, Cellpose: a generalist algorithm for
874 cellular segmentation. *Nat Methods* **18**, 100–106 (2021).

875 69. S. Kaliman, C. Jayachandran, F. Rehfeldt, A.-S. Smith, Limits of Applicability of the
876 Voronoi Tessellation Determined by Centers of Cell Nuclei to Epithelium Morphology.
877 *Front Physiol* **7**, 551 (2016).

878 70. C. Parinot, Q. Rieu, J. Chatagnon, S. C. Finnemann, E. F. Nandrot, Large-Scale
879 Purification of Porcine or Bovine Photoreceptor Outer Segments for Phagocytosis Assays on
880 Retinal Pigment Epithelial Cells. *J Vis Exp*, doi: 10.3791/52100 (2014).

881 71. Y. Mao, S. C. Finnemann, Acute RhoA/Rho Kinase Inhibition Is Sufficient to Restore
882 Phagocytic Capacity to Retinal Pigment Epithelium Lacking the Engulfment Receptor
883 MerTK. *Cells* **10**, 1927 (2021).

884

885 **Acknowledgments**
886 We acknowledge the help of the Flow Cytometry Facility, a core facility of the
887 Interdisciplinary Center for Clinical Research (IZKF) Aachen within the Faculty of
888 Medicine at RWTH Aachen University. We appreciate the technical support of Adam
889 Breitscheidel in the graphic design and Gloria's excellent help in imaging.
890

891 **Funding:**
892 This work in Di Russo's laboratory was supported by:
893 A grant from the Interdisciplinary Centre for Clinical Research within the Faculty of
894 Medicine at the RWTH Aachen University
895 German Research Foundation grant - DFG - (grant nº RU 337 2366/3-1)
896 Mechanobiology in Epithelial 3D Tissue Constructs (ME3T) graduate school (GRK
897 2415/363055819)
898 Additionally, A.N.K is supported by the Add-on Fellowship of the Joachim Herz
899 Foundation
900

901 **Author contributions:**

902 JDR conceived and supervised the project. ANK and TP designed and performed all the
903 experiments. FS and ICD helped establish hiPSC-derived RPE cell culture on PAA gels. FS
904 supported the integrin studies. TPr supported image segmentations and analyses. TH
905 performed and analyzed AFM experiments on decellularised Bruch's membrane. MH and
906 AS contributed to morphometric analyses and interpretation of RPE monolayers *in vivo* and
907 *in vitro*. RW performed the segmentation and analyses of the keratin network. RL provided
908 keratin 8 - YFP mice and expertise on the keratin network. JDR and ANK wrote the
909 manuscript, and all authors discussed and commented on it.
910

911 **Competing interests:**
912 Authors declare that they have no competing interests.
913

914 **Data and materials availability:**
915 All data are available in the main text or the supplementary materials.

**Fig. S1.**

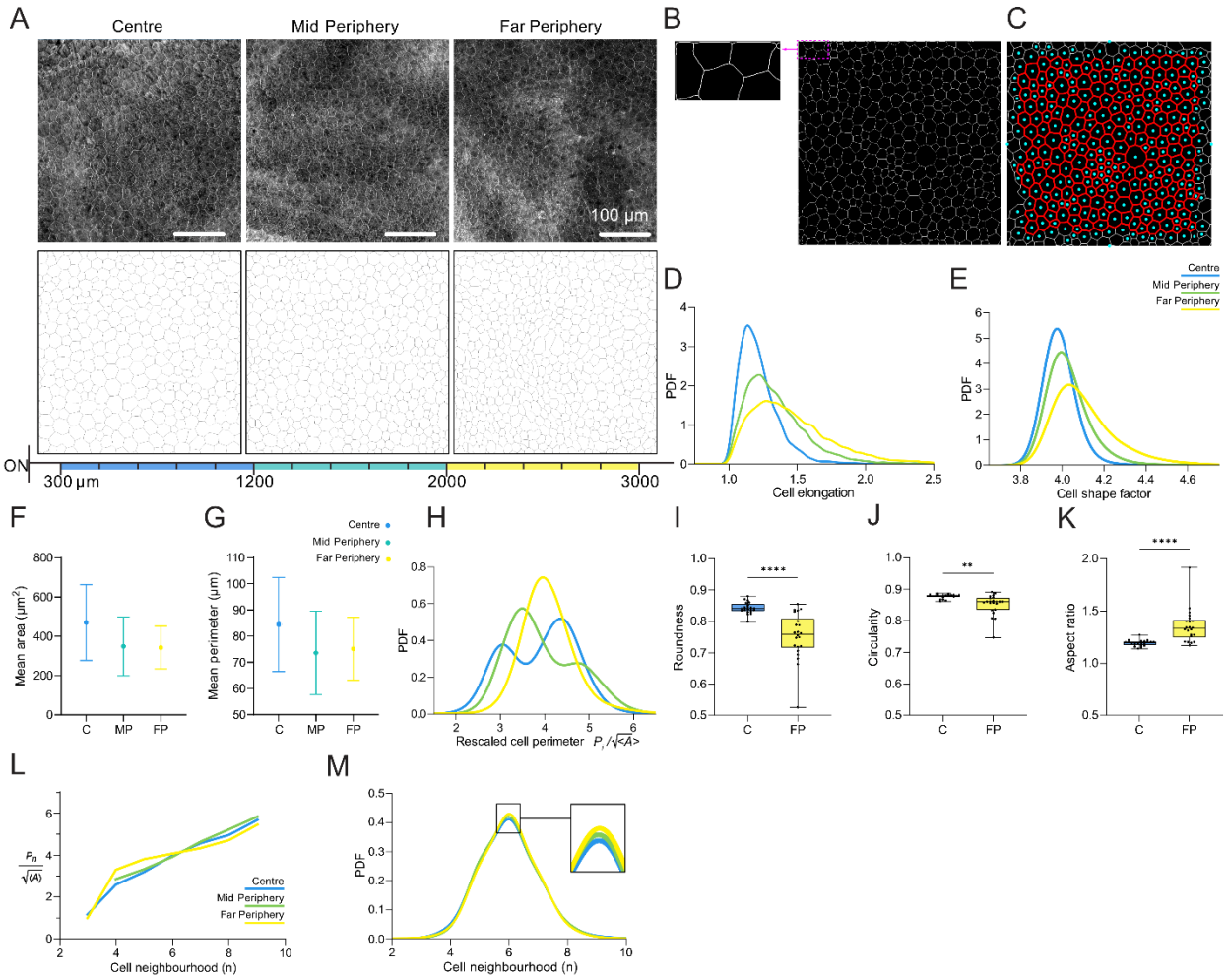


**Fig. S1. Murine RPE represents spatially different monolayer organization. (A)** Representative confocal images of RPE stained for F-actin (top row) and post-processed binary images obtained by skeletonization used for the morphometric characterization upon segmentation (bottom row). Scale bar 100 µm. **(B)** Representative segmentation artefacts generated with Cellpose at the image edge. **(C)** The resulting cells (blue) and neighborhood (red) considered in the analyses. Probability density function (PDF) of cell elongation **(D)** and cell shape factor **(E)** for different retinal regions. The average cellular area **(F)** and perimeter **(G)** shown with mean value and standard deviation for each region, respectively. **(H)** PDF of the rescaled cell perimeters defined as $\boldsymbol{P_i}/\sqrt{<\boldsymbol{A}>}$, Pi being the individual cell perimeter. Nuclear geometric parameters such as roundness **(I)**, circularity **(J)** and elliptical aspect ratio **(K)** show significant difference for cells from center versus far periphery. Topological characteristics of the RPE monolayer such as Desh's law **(L)** representing the relationship between cellular perimeter and shape, and PDF of cell neighborhood **(M)** varying for three different regions. All data were collected from at least 3 mice.

**Fig. S2.**

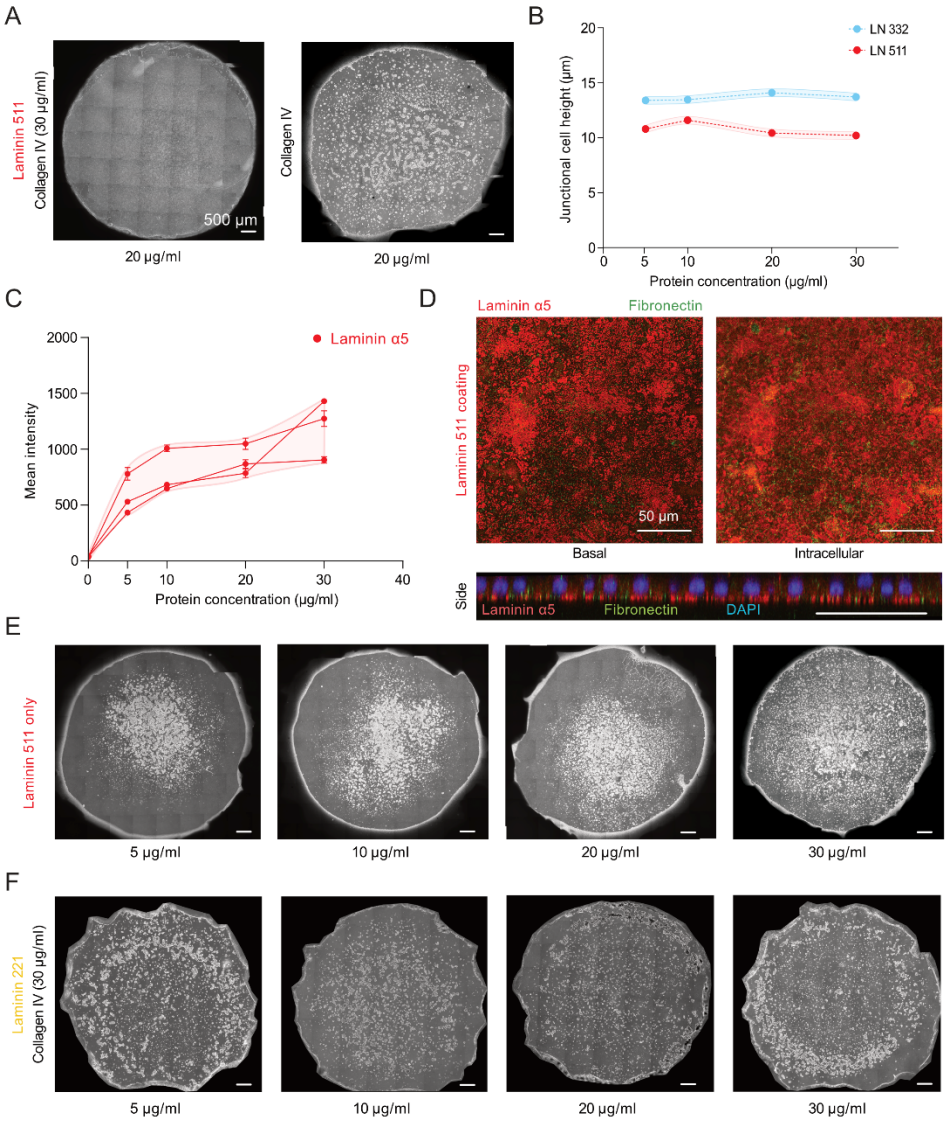


**Fig. S2. Protein composition of polyacrylamide gel surface coating is crucial for cell adhesion strength. (A)** Representative image of complete hiPSC-RPE monolayer obtained on 4 kPa polyacrylamide gel coated with laminin 511 (20 µg/ml) combined with collagen type IV (30 µg/ml) in contrast with the fragmented monolayer on pure collagen type IV (20 µg/ml). Scale bar 500 µm. **(B)** Average cell height measured at the adherence junction levels of one-week old hiPSC-RPE monolayer. Measurements are means from at least three independent experiments ± SEM. **(C)** Line graph of the mean fluorescent intensity of the hydrogel surface fixed and stained with laminin α5 antibody right after chemical crosslinking with different concentrations of laminin 511 combined with collagen type IV (30 µg/ml). This relation indicates correlation between laminin concentration and surface density. Each line represents individual dilution series. Images were taken from 10 different areas of the gel. Data are shown as mean ± SEM. **(D)** Immunofluorescent images of the laminin 511 coated gel surface stained for ECM proteins show the absence of fibronectin protein deposition after one week in cellular culture. Top row represents the signal from laminin α5 (red) and fibronectin (green) at the basal surface and within the monolayer. Fibronectin signal appears to be intracellular as shown in the side view of the monolayer. **(E, F)** Representative overview images of colonies hiPSC-RPE cells seeded on gels coated with different concentrations of laminin 511 and laminin 221 combined with collagen type IV (30 µg/ml), **i**ndicating the insufficient cellular adhesion and monolayer formation in contrast to standard experimental conditions. Scale bar 500 µm.

**Fig. S3.**

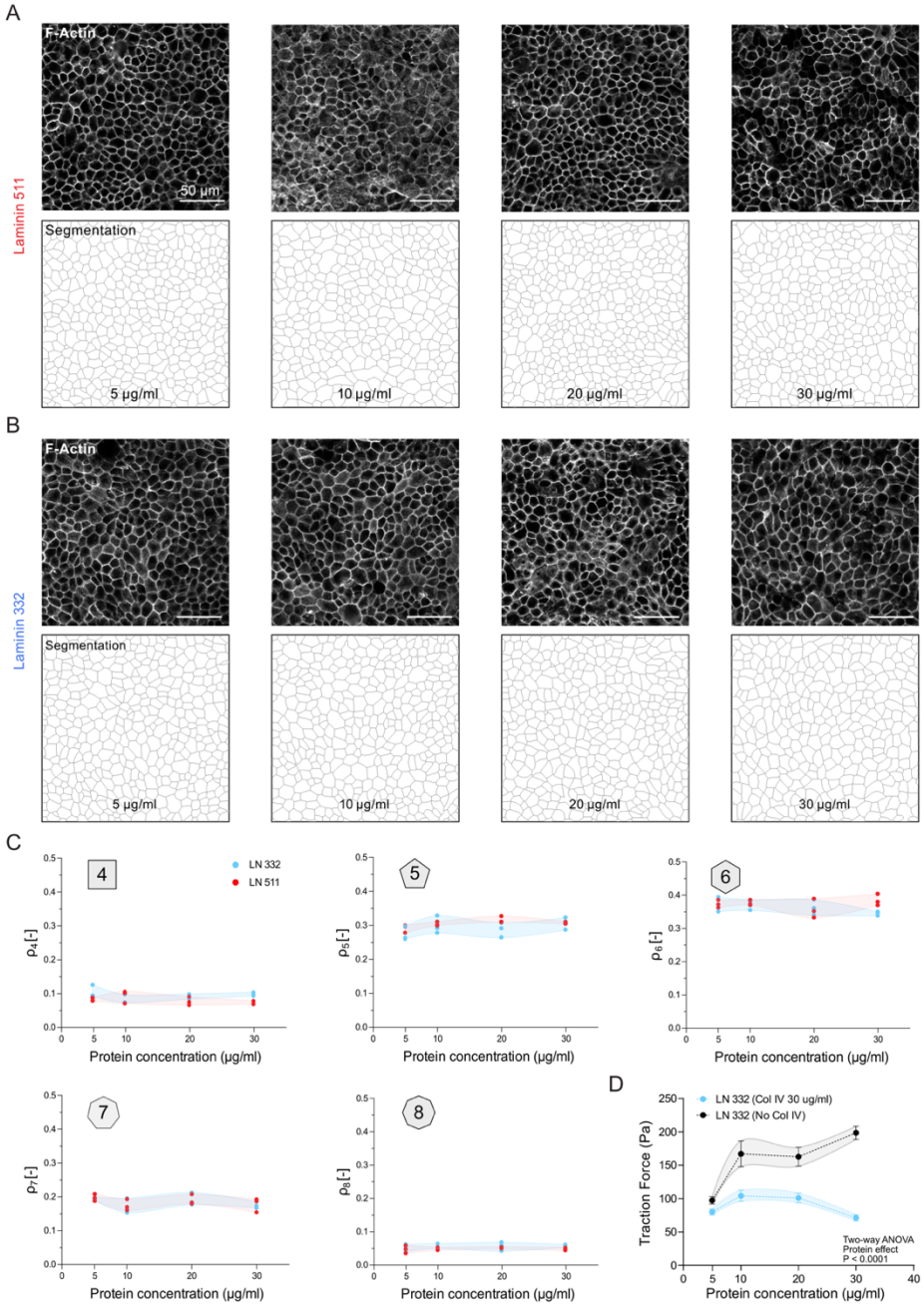


**Fig. S3. Structure and topological stability of RPE *in vitro*.** Representative confocal images of one-week cultured hiPSC-RPE monolayers on 4 kPa PAA gels coated with different concentrations of laminin 511 **(A)** or laminin 332 **(B)** both in presence of collagen type IV (30 µg/ml). The top row represents the actin cytoskeleton network in the stained samples and the bottom row shows segmented images used for morphometric analysis. **(C)** Probabilities of the cellular neighborhood ($\rho_n$) from 4 ($\rho_4$) "squares" to 8 ($\rho_8$) "octagon" indicating the stable neighborhood environment regardless of the protein surface concentration. Data are from 3 independent experiments with 3 independent fields of view in each experiment. **(D)** The presence of collagen type IV in the laminin 332 containing coating solution decreases the traction forces exerted by cells. This difference becomes less significant at lower laminin concentration. Data are shown as mean ± SEM. $P < 0.0001$ for the protein effect using mixed-effects model (REML) with the Geisser-Greenhouse correction and Tuckey's multiple comparisons test.

**Fig. S4.**

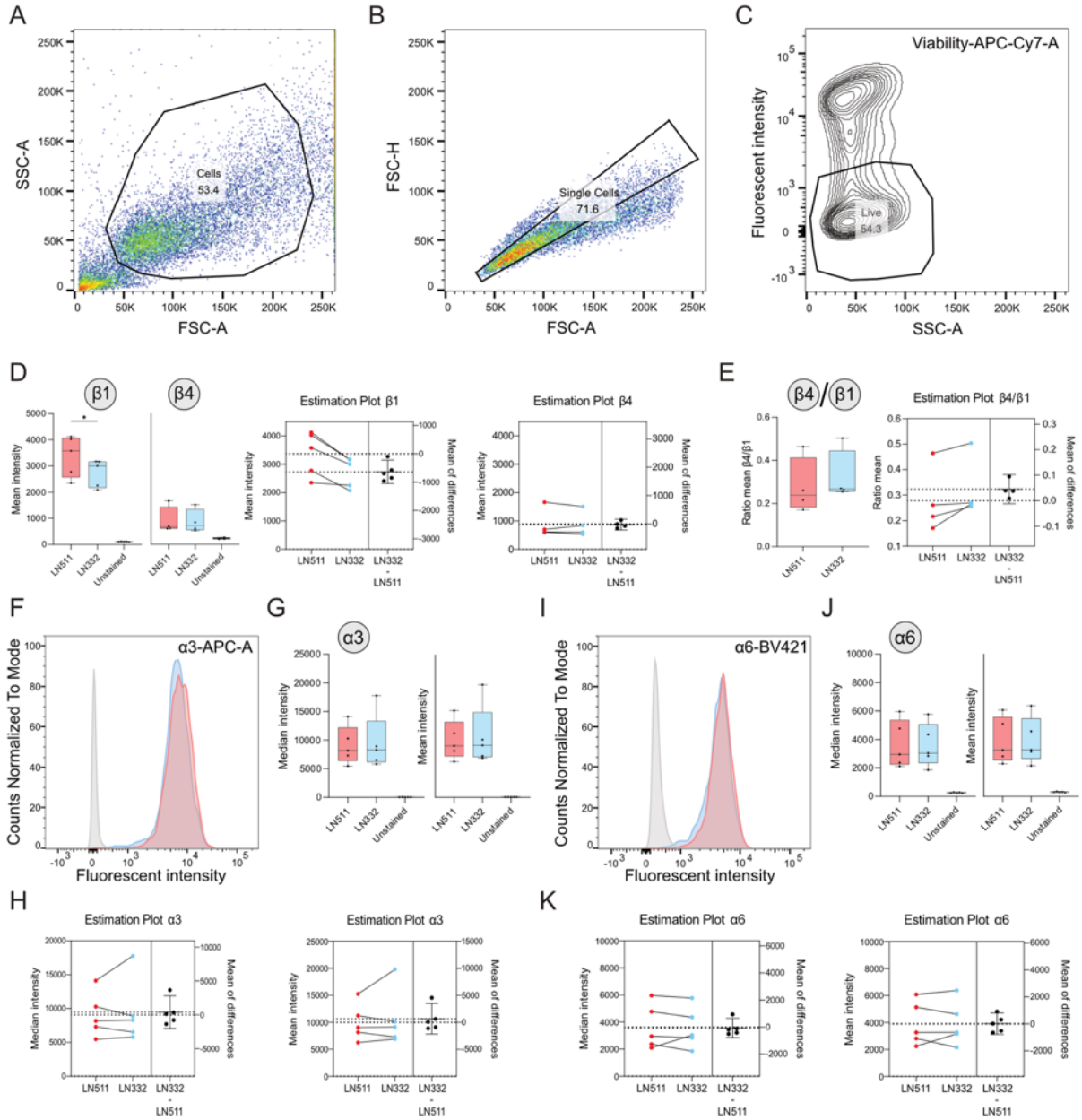


**Fig. S4. Flow cytometry analysis of hiPSC-RPE cultured on polyacrylamide gels coated with 5 µg/ml of laminin 511 or laminin 332.** Representative dot plots showing the gating strategy to identify cells **(A)**, single cells **(B),** contour plot to extract a population of single living cells **(C)** and gating strategy for β4-positive cells **(D)**. **(E)** Box and whisker plots of the mean intensity of integrin β1 and integrin β4 staining (left) and corresponding estimation plots (right) acquired from flow cytometry data. **(F)** Box and whisker (left) and estimation (right) plots showing the ratio between mean intensity of integrin β4 and integrin β1 staining. Representative histograms of flow cytometry analysis, box and whisker plots of median and mean fluorescent intensity and corresponding estimation plots of staining for APC-A-conjugated integrin α3 **(G, H and I)** and BV421-conjugated integrin α6 **(J, K and L)**. The grey-colored histogram represents the signal from unstained cells. Statistical analysis was done using a paired t-test to compare results between laminin 511 and laminin 332 coatings.

983 **Table S 1.**

| Name | Origin | Source | Concentration (µg/ml) / Dilution |
|---|---|---|---|
| **Primary antibodies** | | | |
| Anti mouse laminin 111 (pan-Laminin) | rabbit | Gift from Lydia Sorokin | Rabbit serum, 1:2000 |
| Anti mouse laminin α1 (clone 200) | rat | Gift from Lydia Sorokin | Hybridoma supernatant |
| Anti mouse laminin α2 (clone 4H8-2) | rat | Gift from Lydia Sorokin | Hybridoma supernatant |
| Anti human laminin 332 | rabbit | Gift from Monique Aumailley | Rabbit serum, 1:2000 |
| Anti mouse laminin α4 | rabbit | Gift from Lydia Sorokin | Rabbit serum, 1:1000 |
| Anti mouse laminin α5 | rabbit | Gift from Lydia Sorokin | Rabbit serum, 1:1000 |
| Anti mouse collagen type IV | mouse | Merck Millipore, AB756P | 12.5 |
| Anti mouse collagen type I | rabbit | Novusbio, NB600-408 | 5 |
| Anti mouse elastin | rabbit | Abcam, ab21610 | 5 |
| Phalloidin iFluor 647 | | Abcam, ab176753 | 1:500 |
| Phalloidin iFluor 488 | | Abcam, ab176759 | 1:500 |
| Anti human ZO-1 | rabbit | Thermo Fisher, 61-7300 | 5 |
| Anti human ezrin (clone 3C12) | mouse | Abcam, ab4069 | 20 |
| Anti human fibronectin | rabbit | Sigma, F3648 | 2.5 |
| **Antibodies used for adhesion assay** | | | |
| Integrin β1 (clone P5D2) | mouse | Santa Cruz, sc-13590 L | 2000 (1:100) |
| Integrin β4 (clone ASC-8) | mouse | Merk, MAB2059Z | 1000 (1:50) |
| Integrin αvβ3 (clone LM609) | mouse | Merk, MAB1976Z | 1000 (1:50) |
| Integrin α3 (clone P1B5) | mouse | Merk, MAB1952Z | 1000 (1:50) |
| Integrin α5 (clone P1D6) | mouse | Merk, MAB1956Z | 1000 (1:50) |
| Integrin α6 (clone GOH3) | rat | Santa Cruz, sc-19622 L | 2000 (1:100) |
| **Antibodies used for flow cytometry** | | | |
| Integrin β1-PE (clone 12G10) | mouse | Santa Cruz, sc-59827 PE | 1 mg per million cells |
| Integrin β4-Alexa Flour 488 (clone A9) | mouse | Santa Cruz, sc-13543 AF488 | 1 mg per million cells |
| Integrin α3-Alexa Flour 647 (clone P1B5) | mouse | Santa Cruz, sc-13545 AF647 | 1 mg per million cells |
| Integrin α6-Brilliant Violet 421 (clone GOH3) | rat | BioLegend, 313623 | 5 ml per million cells |
| **Secondary antibodies** | | | |
| Anti-mouse-IgG AF488 | goat | Invitrogen, A11001 | 4 |
| Anti-mouse-IgG AF594 | goat | Invitrogen, A11005 | 4 |
| Anti-mouse-IgG AF647 | goat | Jackson/Dianova, 111-605-144 | 10 |
| Anti-rabbit-IgG AF594 | goat | Invitrogen, A11012 | 4 |
| Anti-rabbit-IgG AF647 | goat | Molecular Probes, A21235 | 10 |
| Anti-rat-IgG AF555 | goat | Invitrogen, A21434 | 4 |
| Anti-rat-IgG AF647 | goat | Thermo Fisher, A21247 | 10 |

984 **Table S1. List of antibodies used in this work.**

985

986 **Table S2.**

| | Laminin 322 | | | Laminin 511 | | |
|---|---|---|---|---|---|---|
| | Exp 1 | Exp 2 | Exp 3 | Exp 1 | Exp 2 | Exp 3 |
| 5 µg/mL | 440 (454) | 638 (654) | 715 (736) | 606 (625) | 686 (710) | 727 (753) |
| 10 µg/mL | 479 (495) | 697 (719) | 654 (679) | 547 (561) | 575 (594) | 396 (415) |
| 20 µg/mL | 627 (641) | 683 (698) | 608 (634) | 559 (572) | 831 (856) | 480 (499) |
| 30 µg/mL | 529 (539) | 325 (334) | 637 (660) | 513 (525) | 710 (737) | 759 (782) |

987
988 **Table S2. Number of cells *in vitro* analyzed for morphometric and topological parameters.**
989
990

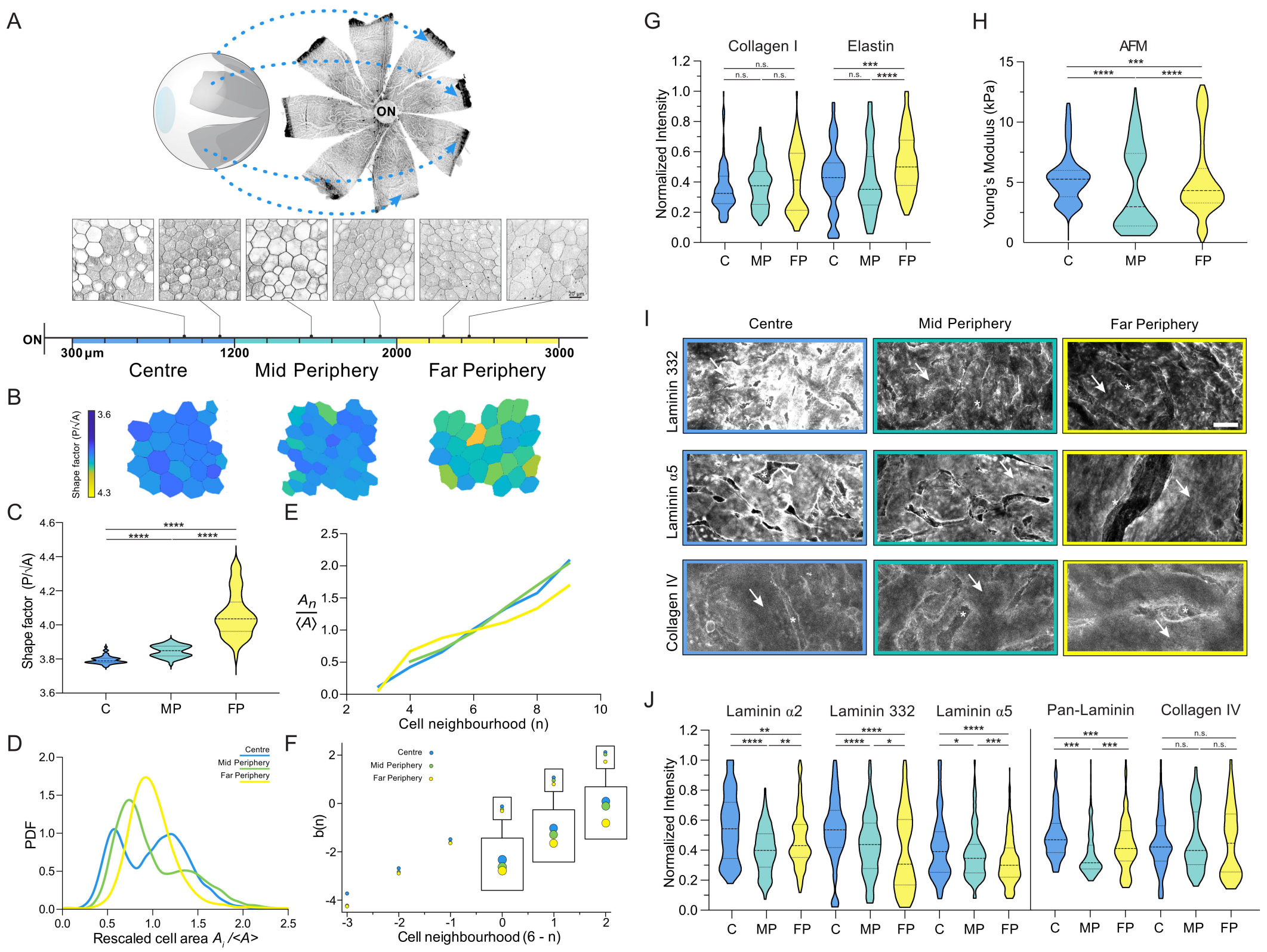
A
ON
300 µm
1200
2000
3000
Centre
Mid Periphery
Far Periphery
B
Shape factor (P/√A)
3.6
4.3
C
Shape factor (P/√A)
C
MP
FP
D
PDF
Rescaled cell area $A_i$ /<A>
Centre
Mid Periphery
Far Periphery
E
$\frac{A_n}{\langle A \rangle}$
Cell neighbourhood (n)
F
b(n)
Cell neighbourhood (6 - n)
G
Collagen I
Elastin
Normalized Intensity
H
AFM
Young's Modulus (kPa)
I
Centre
Mid Periphery
Far Periphery
Laminin 332
Laminin α5
Collagen IV
J
Laminin α2
Laminin 332
Laminin α5
Pan-Laminin
Collagen IV
Normalized Intensity

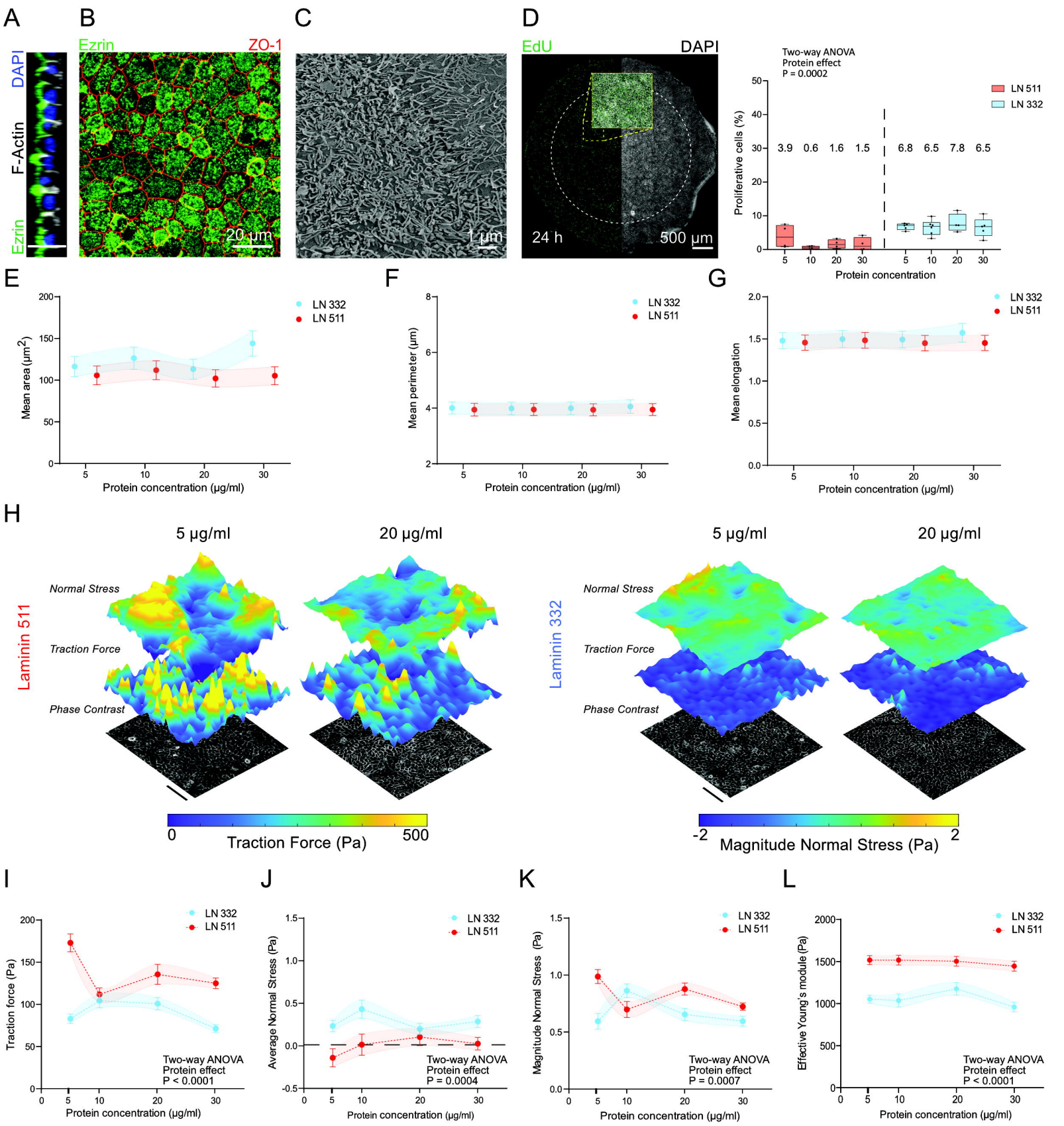
A
B
C
D
DAPI
F-Actin
Ezrin
Ezrin
ZO-1
20 µm
1 µm
EdU
DAPI
24 h
500 µm
Two-way ANOVA
Protein effect
P = 0.0002
LN 511
LN 332
Proliferative cells (%)
3.9 0.6 1.6 1.5
6.8 6.5 7.8 6.5
Protein concentration
E
Mean area (µm²)
Protein concentration (µg/ml)
F
Mean perimeter (µm)
G
Mean elongation
H
5 µg/ml
20 µg/ml
Laminin 511
Laminin 332
Normal Stress
Traction Force
Phase Contrast
Traction Force (Pa)
Magnitude Normal Stress (Pa)
I
Traction force (Pa)
Two-way ANOVA
Protein effect
P < 0.0001
J
Average Normal Stress (Pa)
Two-way ANOVA
Protein effect
P = 0.0004
K
Magnitude Normal Stress (Pa)
Two-way ANOVA
Protein effect
P = 0.0007
L
Effective Young's module (Pa)
Two-way ANOVA
Protein effect
P < 0.0001

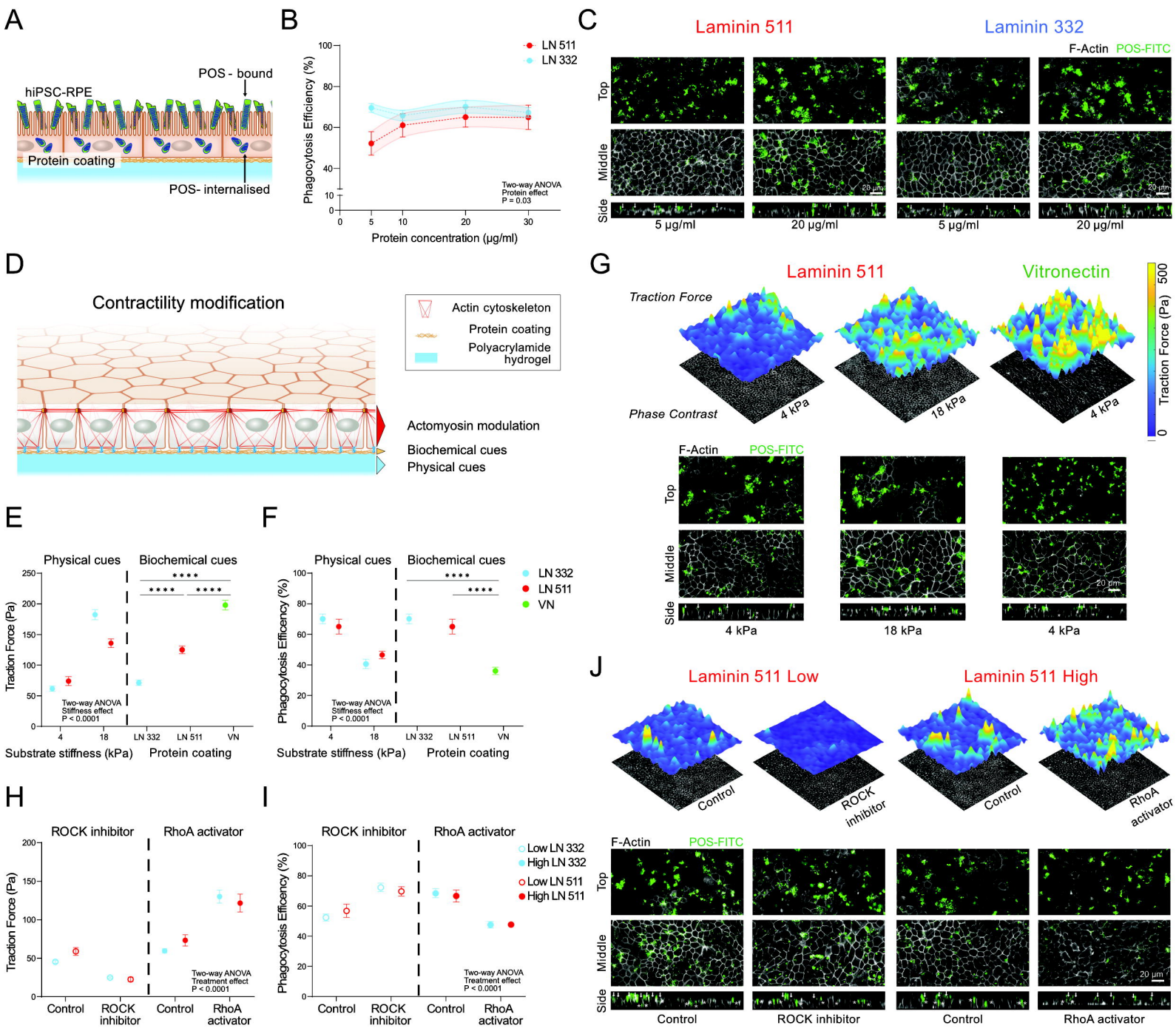
A
hiPSC-RPE
POS - bound
Protein coating
POS- internalised
B
LN 511
LN 332
Phagocytosis Efficiency (%)
Protein concentration (µg/ml)
Two-way ANOVA
Protein effect
P = 0.03
C
Laminin 511
Laminin 332
F-Actin POS-FITC
Top
Middle
Side
20 µm
5 µg/ml
20 µg/ml
5 µg/ml
20 µg/ml
D
Contractility modification
Actin cytoskeleton
Protein coating
Polyacrylamide hydrogel
Actomyosin modulation
Biochemical cues
Physical cues
G
Laminin 511
Vitronectin
Traction Force
Phase Contrast
4 kPa
18 kPa
4 kPa
Traction Force (Pa)
500
0
F-Actin POS-FITC
Top
Middle
Side
20 µm
4 kPa
18 kPa
4 kPa
E
Physical cues
Biochemical cues
Traction Force (Pa)
Two-way ANOVA
Stiffness effect
P < 0.0001
Substrate stiffness (kPa)
Protein coating
F
Physical cues
Biochemical cues
LN 332
LN 511
VN
Phagocytosis Efficiency (%)
Two-way ANOVA
Stiffness effect
P < 0.0001
Substrate stiffness (kPa)
Protein coating
J
Laminin 511 Low
Laminin 511 High
Control
ROCK inhibitor
Control
RhoA activator
F-Actin POS-FITC
Top
Middle
Side
20 µm
Control
ROCK inhibitor
Control
RhoA activator
H
ROCK inhibitor
RhoA activator
Traction Force (Pa)
Two-way ANOVA
Treatment effect
P < 0.0001
Control
ROCK inhibitor
Control
RhoA activator
I
ROCK inhibitor
RhoA activator
Low LN 332
High LN 332
Low LN 511
High LN 511
Phagocytosis Efficiency (%)
Two-way ANOVA
Treatment effect
P < 0.0001
Control
ROCK inhibitor
Control
RhoA activator

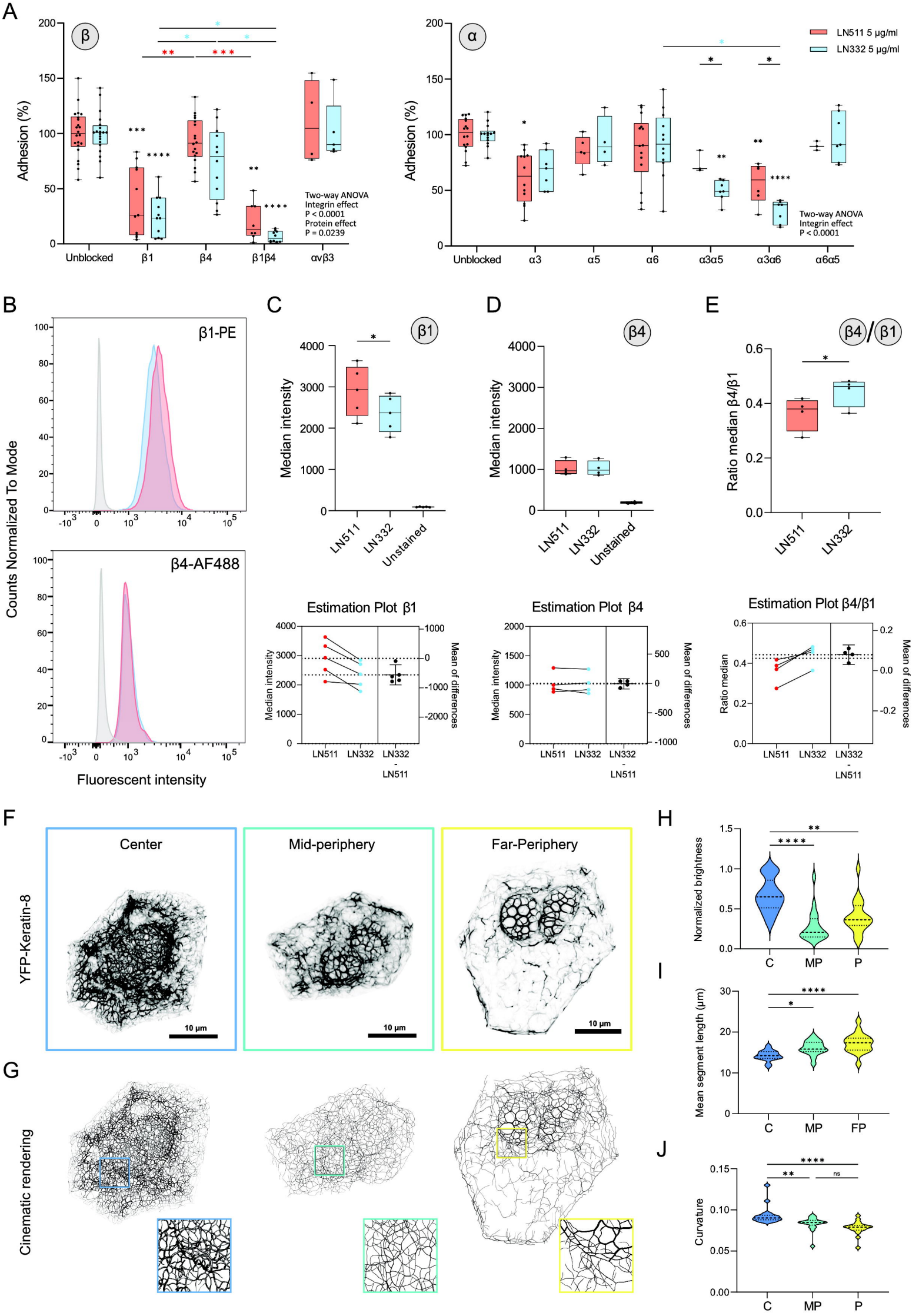
A
β
Adhesion (%)
Unblocked
β1
β4
β1β4
αvβ3
Two-way ANOVA
Integrin effect
P < 0.0001
Protein effect
P = 0.0239
α
LN511 5 µg/ml
LN332 5 µg/ml
Unblocked
α3
α5
α6
α3α5
α3α6
α6α5
Two-way ANOVA
Integrin effect
P < 0.0001
B
β1-PE
β4-AF488
Counts Normalized To Mode
Fluorescent intensity
C
β1
Median intensity
LN511
LN332
Unstained
Estimation Plot β1
Mean of differences
D
β4
Estimation Plot β4
E
β4/β1
Ratio median β4/β1
Estimation Plot β4/β1
Ratio median
F
Center
Mid-periphery
Far-Periphery
YFP-Keratin-8
10 µm
G
Cinematic rendering
H
Normalized brightness
C
MP
P
I
Mean segment length (µm)
FP
J
Curvature
ns

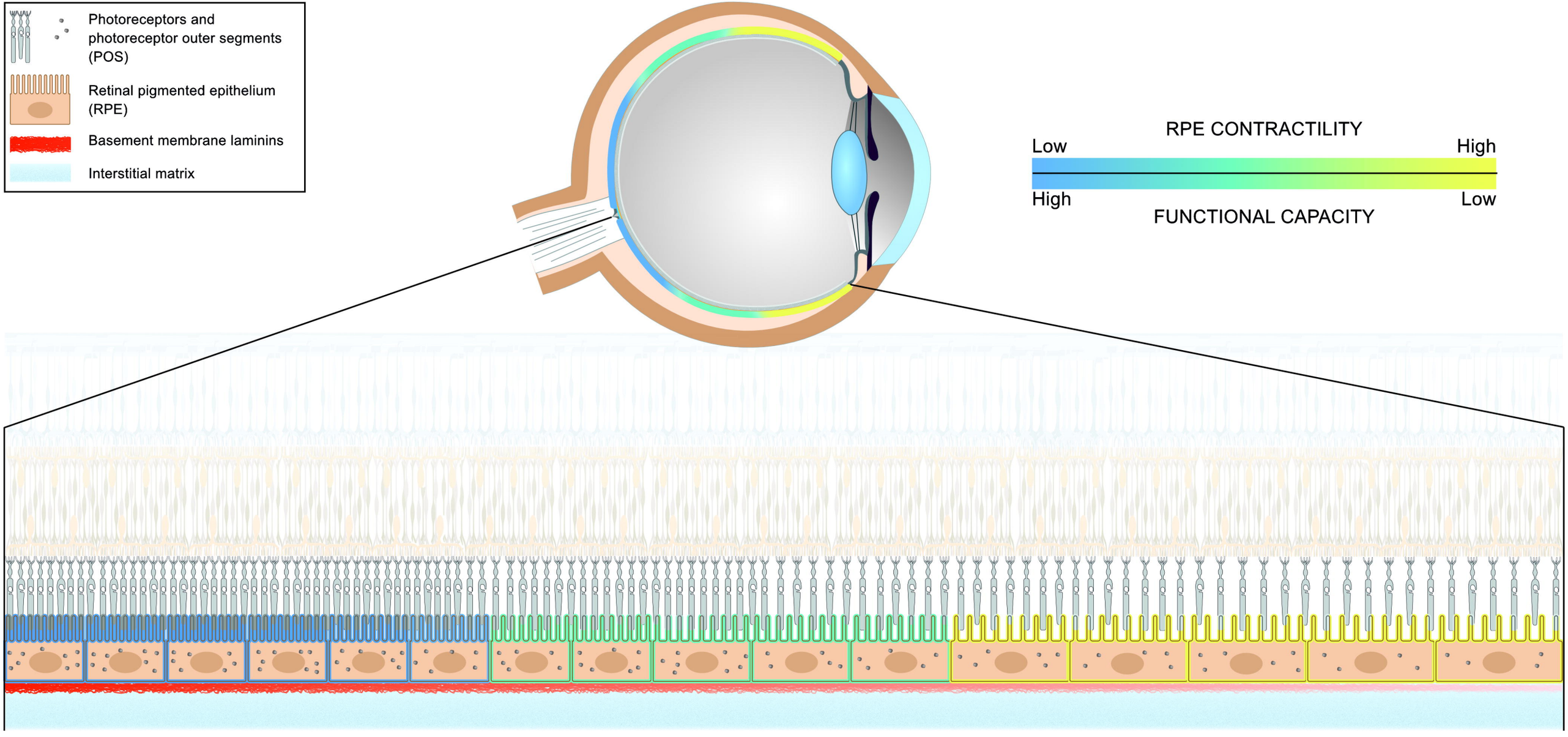
Photoreceptors and photoreceptor outer segments (POS)
Retinal pigmented epithelium (RPE)
Basement membrane laminins
Interstitial matrix
RPE CONTRACTILITY
Low
High
High
Low
FUNCTIONAL CAPACITY